SIAM J. SCI. COMPUT.
Vol. 44, No. 2, pp. B368–B394

HIGH ORDER SEMI-IMPLICIT WENO SCHEMES FOR ALL-MACH FULL EULER SYSTEM OF GAS DYNAMICS*

SEBASTIANO BOSCARINO†, JINGMEI QIU‡, GIOVANNI RUSSO†, AND TAO XIONG§

Abstract. In this paper, we propose a new high order semi-implicit scheme for the all-Mach full Euler equations of gas dynamics. Material waves are treated explicitly, while acoustic waves are treated implicitly, thus avoiding severe CFL restrictions for low Mach flows. High order accuracy in time is obtained by a semi-implicit temporal integrator based on the IMEX Runge–Kutta (IMEX-RK) framework. High order in space is achieved by finite difference WENO schemes with characteristic-wise reconstructions adapted to the semi-implicit IMEX-RK time discretization. Type A IMEX schemes are constructed to handle non-well-prepared initial conditions. Besides, these schemes are proven to be asymptotic preserving and asymptotically accurate as the Mach number vanishes for well-prepared initial conditions. The divergence-free property of the time-discrete schemes is proved. The proposed scheme can also well capture discontinuous solutions in the compressible regime, especially for two-dimensional Riemann problems. Numerical tests in one and two space dimensions will illustrate the effectiveness of the proposed schemes.

Key words. all-Mach number, full Euler equations, asymptotic preserving, asymptotically accurate, finite difference WENO, characteristicwise reconstruction

AMS subject classifications. 35L65, 35B40, 35C20, 76N15, 76M20, 76M45, 76B47, 65M06

DOI. 10.1137/21M1424433

1. Introduction.

Computational fluid dynamics has been a very active research field in past decades. Numerical methods developed in this area generally can be divided into two categories, which are classified by the dimensionless Mach number. For moderate to high Mach number compressible effects have to be taken into account, while for low Mach number the flow can be considered incompressible or weakly compressible. For compressible flows, most numerical solutions are obtained by Godunov type shock capturing schemes for compressible Euler equations, which have the structure of a hyperbolic system of conservation laws [36, 47, 23, 43, 15], while for the incompressible flows, preserving incompressibility and resolving vortex dynamics are among the main purposes [13, 46, 24].

*Submitted to the journal's Computational Methods in Science and Engineering section June 3, 2021; accepted for publication (in revised form) October 14, 2021; published electronically April 4, 2022.

https://doi.org/10.1137/21M1424433

Funding: The first and third authors are supported by the Italian Ministry of Instruction, University and Research (MIUR), with funds coming from PRIN Project 2017 (2017KKJP4X, entitled "Innovative numerical methods for evolutionary partial differential equations and applications"). The first author has been supported by the University of Catania (Piano della Ricerca 2016/2018, Linea di intervento 2). The first and third authors are members of the INdAM Research group GNCS. The second author is supported by NSF grant NSF-DMS-1818924 and Air Force Office of Scientific Research grant FA9550-18-1-0257. The third author has been supported by ITN-ETN Horizon 2020 Project ModCompShock, Modeling and Computation on Shocks and Interfaces, Project Reference 642768. The fourth author is supported by NSFC 11971025, NSF of Fujian Province 2019J06002, Strategic Priority Research Program of Chinese Academy of Sciences grant XDA25010401.

†Department of Mathematics and Computer Science, University of Catania, Catania, 95125, Italy (boscarino@dmi.unict.it, russo@dmi.unict.it).

‡Department of Mathematics, University of Delaware, Newark, DE 19716 USA (jingqiu@udel.edu).

§Corresponding author. School of Mathematical Sciences, Fujian Provincial Key Laboratory of Mathematical Modeling and High-Performance Scientific Computing, Xiamen University, Xiamen, Fujian, 361005, People's Republic of China (txiong@xmu.edu.cn).

There are, however, circumstances in which flows with a wide range of Mach number appear, making it desirable to develop numerical methods which can be applied for fluid flows at any speed, as already shown in the pioneering work of Harlow and Amdsen [28, 29]. However, due to the different physical mechanisms and mathematical characteristics for the governing equations at different speeds, the development of efficient and effective numerical methods to capture flows with different compressibility is challenging [34, 20, 41], and a lot of progress has been made only recently. For hyperbolic systems, waves propagate at finite speeds. Numerical methods have to resolve all the space and time scales that characterize these waves. Most shock capturing schemes devoted to such systems are obtained by explicit time discretization, and the time step has to satisfy a stability restriction, known as the CFL condition: it is limited by the size of the spatial mesh divided by the fastest wave speed. For compressible flows with Mach number greater than, say, 0.1, such a restriction is not a problem: indeed, if one is interested in resolving all the waves, accuracy and stability restrictions on space and time discretization are of a similar nature. However, for low Mach flows, acoustic waves usually carry a negligible amount of energy. If one is not interested in resolving them, then the system becomes *stiff*: stability limitations on the time step are much stricter than the restrictions imposed by accuracy [48, 49]. In such cases, one may resort to implicit time discretization to avoid the acoustic CFL restriction. However, shock capturing schemes are highly nonlinear, and a *naive* implicit version of them risks being very inefficient. Furthermore, numerical viscosities for Godunov-type schemes are inversely proportional to the Mach number, introducing excessive numerical dissipations on the slow waves [19]. Preconditioning techniques are adopted to cure the large numerical diffusion as discussed in [48, 50, 37], but such techniques are effectively applicable only if Mach numbers are not too small.

On the other hand, as the Mach number vanishes, the flow converges to the incompressible limit. For the full Euler equations, at the incompressible limit, the density remains constant along the fluid particle trajectories, and the pressure waves propagate with infinite speed. The energy conservation equation reduces to the incompressibilty condition $\nabla \cdot \mathbf{u} = 0$ on the velocity field [14], so that the pressure and the density are decoupled. The pressure turns out to act as a Lagrange multiplier to enforce incompressibility of the flow [34]. A rigorous proof for the compressible flow converging to the incompressible one as the Mach number goes to zero is given in [32]. An effective approach to deal with low Mach flows is given by pressure-based algorithms, such as, for example, the one by Casulli and Greenspan [12], in which a semi-implicit treatment of the pressure is incorporated in a scheme for compressible flow. The authors use an upwind discretization on the material wave, and an implicit equation for the pressure, which is solved by an SOR-type method. Several authors have subsequently worked on the development of semi-implicit methods [34, 38] based on low-Mach asymptotics [32]. However, many such schemes are specifically designed to deal with low Mach flows. When the fluid flow is compressible at large speed, shock discontinuities may form and propagate. In these cases, it is necessary to resort to conservative schemes (density-based schemes) which correctly capture possible shocks.

Recently several papers have been written along these lines; see, for example, [18, 25, 44, 22, 9, 8] for isentropic Euler and Navier–Stokes equations, or [16, 45, 21, 51, 20, 10] for full Euler and Navier–Stokes equations. However, most finite volume and finite difference schemes for full Euler equations are second order accurate in space and time, while existing high order schemes developed for all-Mach flows in isentropic Euler equations are not robust enough to be directly extended to the full Euler equations.

The aim of the present paper is to design a new high order finite difference shock capturing scheme for the full compressible Euler equations. Finite difference weighted essentially non-oscillatory (WENO) schemes are used for spatial discretization, while high order semi-implicit IMEX Runge–Kutta (SI-IMEX-RK) methods are adopted for time discretization. New IMEX schemes are suitably designed for stability and accuracy, with time stepping size independent of the Mach number ε. A key feature of the scheme is the implicit treatment of acoustic waves, while material waves are treated explicitly by WENO reconstructions of numerical fluxes. In particular, a suitable local Lax–Friedrich flux with characteristicwise WENO reconstruction has been adopted for the explicit convective terms, while componentwise WENO reconstructions with zero numerical diffusion is used for implicit acoustic terms. The method is able to capture shocks and discontinuities in an essentially non-oscillatory fashion in the compressible regime. In order to avoid the nonlinearity from the equation of state (EOS), a semi-implicit treatment similar to the one adopted in [9] is used, leading to a linearized elliptic equation for the pressure, as described in section 3.2. Another essential ingredient of the scheme design is to split the pressure into a thermodynamic pressure and a hydrodynamic one, using a similar idea adopted in [16] but with a fixed splitting parameter α. The thermodynamic pressure is used for the characteristic reconstructions, while the hydrodynamic pressure is obtained by solving an elliptic system. We show that the resulting scheme is asymptotic preserving (AP) and asymptotically accurate [30, 31], i.e., it is a consistent and high order discretization of the compressible Euler equations and, in the limit as $\varepsilon \to 0$, with Δx and Δt fixed, it becomes a consistent and high order discretization of the incompressible Euler equations.

The rest of the paper is organized as follows. We recall the low Mach limit for the full compressible Euler equations in section 2. We start section 3 by introducing a first order semi-implicit scheme in time, then we describe the extension to high order time discretization using IMEX methods in section 3.2; in particular we design IMEX methods called type A [1], which will be robust enough to solve the elliptic equation for the pressure. We close the section with a description of high order spatial discretization obtained by characteristicwise and componentwise WENO strategies. The AP and asymptotic accuracy (AA) properties of the scheme are given in section 4. Numerical tests are performed in section 5, with the conclusion drawn in the last section.

2. Low Mach limit for the full Euler equations. We consider the compressible Euler equations for an ideal gas in the nondimensional form [39, 19, 16]

$$\begin{cases} \rho_t + \nabla \cdot (\rho \mathbf{u}) = 0, \\ (\rho \mathbf{u})_t + \nabla \cdot (\rho \mathbf{u} \otimes \mathbf{u}) + \frac{1}{\varepsilon^2} \nabla p = 0, \\ E_t + \nabla \cdot [(E+p)\mathbf{u}] = 0, \end{cases} \tag{2.1}$$

with the EOS for a polytropic gas satisfying

$$E = \frac{p}{\gamma - 1} + \frac{\varepsilon^2}{2} \rho |\mathbf{u}|^2, \tag{2.2}$$

where $\gamma > 1$ is the ratio of specific heats. The parameter ε represents a global Mach number characterizing the nondimensionalization. System (2.1) is *hyperbolic* and the eigenvalues along the direction $\mathbf{n}$ are $\lambda_1 = \mathbf{u} \cdot \mathbf{n} - c_s/\varepsilon$, $\lambda_2 = \mathbf{u} \cdot \mathbf{n}$, $\lambda_3 = \mathbf{u} \cdot \mathbf{n} + c_s/\varepsilon$ with $c_s = \sqrt{\gamma p/\rho}$.

When the reference Mach number is of order one, namely $\varepsilon = \mathcal{O}(1)$, modern shock capturing methods are able to compute the formation and evolution of shocks and other complex structures with high resolutions at a reasonable cost. On the other hand, when the flows are slow compared to the speed of sound, i.e., $\varepsilon \ll 1$, we are near the incompressible regime. In such a situation, pressure waves become very fast compared to material waves. Standard explicit shock-capturing methods require a CFL time restriction dictated by the sound speed c_s/ε to integrate the system. This leads to stiffness in time (see, e.g., [25, 18, 16]), where the time discretization is constrained by a stability condition given by $\Delta t < \Delta x/\lambda_{\max} = \mathcal{O}(\varepsilon \Delta x)$, where Δt is the time step size, Δx is the mesh size, and $\lambda_{\max} = \max_\Omega(|\mathbf{u}| + c_s/\varepsilon)$ on the computational domain Ω. This restriction results in an increasingly large computational time for low Mach fluid flows. Moreover, excessive numerical viscosity (scales as ε^{-1}) in standard upwind schemes leads to highly inaccurate solutions [48, 49]. Thus, it is a challenge and of great importance to design numerical schemes, not only for shock-capturing, but also with consideration on stability and consistency in the incompressible limit, i.e., with the AP property. In fact, in the low Mach limit, one is not interested in resolving the pressure waves; instead the fluid pressure serves as a Lagrangian multiplier in preserving the incompressibility of the velocity field. For the theoretical analysis of convergence from compressible flow to incompressible equations, such as $\varepsilon \to 0$, we refer to Klainerman and Majda [32, 33] for a rigorous study in this low Mach limit.

Here we recall the classical formal derivation of the incompressible Euler equations from the rescaled compressible Euler equations for an ideal gas (2.1) with the EOS (2.2). We consider an asymptotic expansion *ansatz* for the two main variables,

$$\begin{aligned} p(\mathbf{x},t) &= p_0(\mathbf{x},t) + \varepsilon^2\, p_2(\mathbf{x},t) + \cdots, \\ u(\mathbf{x},t) &= \mathbf{u}_0(\mathbf{x},t) + \varepsilon\, \mathbf{u}_1(\mathbf{x},t) + \cdots, \end{aligned} \tag{2.3}$$

and insert them into the full Euler equations (2.1). First, for the leading order $\mathcal{O}(\varepsilon^{-2})$, we formally find $\nabla p_0(\mathbf{x},t) = 0$, i.e., pressure p_0 is constant in space, up to fluctuations of $\mathcal{O}(\varepsilon^2)$, and by (2.2), assuming E has a similar expansion as p in (2.3), we get $E_0 = p_0/(\gamma - 1)$. Then we formally find, up to $\mathcal{O}(1)$

$$\begin{cases} \partial_t \rho_0 + \nabla \cdot (\rho_0 \mathbf{u}_0) \;=\; 0, \\ \partial_t(\rho_0 \mathbf{u}_0) + \nabla \cdot (\rho_0 \mathbf{u}_0 \otimes \mathbf{u}_0) + \nabla p_2 \;=\; 0, \\ \partial_t E_0 + \nabla \cdot [(E_0 + p_0)\mathbf{u}_0] \;=\; 0. \end{cases} \tag{2.4}$$

From the energy equation in (2.4), with the EOS (2.2) and denoting $d/dt = \partial/\partial t + \mathbf{u}_0 \cdot \nabla$, we have

$$\nabla \cdot \mathbf{u}_0 = -\frac{1}{p_0 \gamma} \frac{dp_0}{dt}. \tag{2.5}$$

Now integrating (2.5) over a spatial domain Ω with no-slip or periodic boundary conditions, we get $\int_\Omega \nabla \cdot \mathbf{u}_0 \, d\mathbf{x} = \int_{\partial\Omega} \mathbf{u}_0 \cdot \mathbf{n} \, ds = 0$, where $\mathbf{n}$ is the unit outward normal vector along $\partial\Omega$, and this implies p_0 is constant in both space and time, i.e., $p_0 = \text{Const}$. Then, back into (2.5), one finds the divergence constraint $\nabla \cdot \mathbf{u}_0 = 0$ in the zero Mach number limit. In summary, we have

$$\begin{cases} p_0 = \text{Const.}, \quad \nabla \cdot \mathbf{u}_0 = 0, \\ \partial_t \rho_0 + \nabla \cdot (\rho_0 \mathbf{u}_0) = 0, \\ \partial_t (\rho_0 \mathbf{u}_0) + \nabla \cdot (\rho_0 \mathbf{u}_0 \otimes \mathbf{u}_0) + \nabla p_2 = 0. \end{cases} \tag{2.6}$$

As a direct consequence of $\nabla \cdot \mathbf{u}_0 = 0$, we obtain from the mass-continuity equation $d\rho/dt = 0$, namely the material derivative of the density is zero. This means that the density is constant along the particle trajectories. In particular, if the initial density is constant in space, the density of the fluid is constant in space and time. Note that

$$p_2 = \lim_{\varepsilon \to 0} \frac{1}{\varepsilon^2}(p - p_0) \tag{2.7}$$

is implicitly defined by the constraint $\nabla \cdot \mathbf{u}_0 = 0$, which satisfies the following elliptic equation:

$$-\nabla \cdot \left(\frac{1}{\rho_0} \nabla p_2 \right) = \nabla \cdot ((\mathbf{u}_0 \cdot \nabla)\mathbf{u}_0). \tag{2.8}$$

Finally, we assume the initial condition is *well-prepared* [32, 33, 19, 34], that is, the initial condition for (2.3) is compatible with the equations at various orders of ε:

$$\begin{cases} p(t=0, \mathbf{x}) = p_0 + \varepsilon^2 \, p_2(0, \mathbf{x}) + \cdots, \\ \mathbf{u}(t=0, \mathbf{x}) = \mathbf{u}_0(\mathbf{x}) + \mathcal{O}(\varepsilon), \end{cases} \tag{2.9}$$

with $p_0 = \text{Const.}$ and $\nabla \cdot \mathbf{u}_0 = 0$ and we impose $\rho(0, \mathbf{x}) = \rho_0(\mathbf{x})$, with $\rho_0(\mathbf{x})$ being a strictly positive function. Note that well-prepared initial conditions are required if we want the solution to the ε-dependent problem to smoothly converge to the solution of the limiting incompressible problem. Furthermore, a well-prepared initial condition is an important requirement to design AP schemes. It is crucial to preserve the constant state for leading order terms of p and E, as well as the divergence-free constraint on the leading order term of $\mathbf{u}$. For an arbitrary initial condition, an initial layer will appear, which requires a numerical resolution at the ε-scale.

3. Numerical scheme. In this section, we aim to construct and analyze a class of high order finite difference schemes with the AP property for unsteady compressible flows, when the Mach number ε spans several orders of magnitude. The features of our scheme are the following: we design a semi-implicit IMEX (SI-IMEX) time discretization strategy, so that the scheme is stable with a time stepping constraint independent of the Mach number ε, the AP property is preserved in the zero Mach number limit, and the scheme can be implemented in a semi-implicit manner [4, 3, 2, 5] to enable effective and efficient numerical implementations. Our scheme preserves the incompressible velocity field in the zero Mach number limit by involving an elliptic solver for the hydrostatic pressure. In this section, the strategy of numerical discretizations is different from the traditional *method-of-lines* approach, since we first perform time discretization to ensure the AP property, after which we apply a suitable space discretization. In particular we adopt high order WENO strategies with characteristic reconstructions tailored to IMEX-type methods in time. The final scheme can successfully capture shocks in the compressible regime and efficiently solve the equations in the low Mach regime, with CFL condition depending only on fluid velocity.

3.1. Semi-implicit treatment. We introduce our proposed strategy of implicit and explicit time discretizations, which is similar in spirit to the first order scheme in [16] with a slight modification. We emphasize the special treatment to avoid solving nonlinear equations required by a fully implicit scheme. We rewrite (2.1) as

$$\frac{dU}{dt} = -\nabla \cdot \mathcal{F}_E - \nabla \cdot \mathcal{F}_{SI}, \tag{3.1}$$

where $U = (\rho, \rho\mathbf{u}, E)^T$ and

$$\mathcal{F}_E \doteq \begin{pmatrix} \mathbf{q}_E \\ \left(\frac{\mathbf{q}_E \otimes \mathbf{q}_E}{\rho_E}\right) + \alpha\, p_E \mathbb{I} \\ 0 \end{pmatrix}, \qquad \mathcal{F}_{SI} \doteq \begin{pmatrix} 0 \\ \frac{1-\alpha\varepsilon^2}{\varepsilon^2} p_I \mathbb{I} \\ \frac{E_E + p_E}{\rho_I} \mathbf{q}_I \end{pmatrix}. \tag{3.2}$$

Subscripts E and SI of $\mathcal{F}$ indicate the explicit and semi-implicit treatment of the first and the second term, respectively. Several remarks are in order:

1. The parameter α determines the splitting between the explicit and implicit contribution of the pressure: the former ensures that the explicit part is still hyperbolic, with a much smaller sound speed than the physical one, when $\varepsilon \ll 1$, while the latter will ensure much milder stability restrictions. As ε increases, the explicit contribution becomes more and more relevant. This form of splitting is similar to the one in [16] but differs in two main aspects: one is the implicit treatment of ρ in the energy equation in (3.2), which gives a better AP property, as will be elaborated in section 4; the other is the choice of the parameter α in splitting the pressure. In [16], α is chosen depending on the Mach number ε. In our proposed scheme, however, α is chosen to be equal to 1 for all $\varepsilon < 1$, and $\alpha = 1/\varepsilon^2$ for $\varepsilon \geq 1$.
2. We use the following EOS for (2.2) to avoid the nonlinearity in the semi-implicit scheme:

$$E_E = \frac{1}{\gamma - 1} p_E + \varepsilon^2 \frac{|\mathbf{q}_E|^2}{2\rho_E}, \quad E_I = \frac{1}{\gamma - 1} p_I + \varepsilon^2 \frac{|\mathbf{q}_E|^2}{2\rho_E}. \tag{3.3}$$

   The subscripts E and I of $\mathbf{q}$, ρ, E, and p indicate the explicit and implicit treatments of the corresponding variables, respectively.
3. For the implicit term p_I in (3.2), it is convenient to introduce a pressure perturbation $p_{I,2}$ [41], corresponding to the hydrodynamic pressure in the incompressible limit, defined as

$$p_{I,2} \doteq \frac{p_I - \bar{p}_E}{\varepsilon^2}, \tag{3.4}$$

   where $\bar{p}_E$ denotes the spatial average of the pressure p_E computed from the EOS (3.3). In this way the term $p_{I,2}$ will remain finite even as $\varepsilon \to 0$. Then we have

$$\frac{1}{\varepsilon^2} \nabla p_I = \nabla p_{I,2}. \tag{3.5}$$

As an example, we present the scheme as well as the flow chart to update the numerical solution $U^{n+1} = (\rho^{n+1}, \mathbf{q}^{n+1}, E^{n+1})^T$ for the first order semi-implicit scheme solving

system (2.1). We focus on the time discretization while keeping the space continuous, whose discretizations will be discussed in detail in section 3.3:

$$\frac{\rho^{n+1}-\rho^n}{\Delta t}+\nabla\cdot\mathbf{q}^n=0, \tag{3.6a}$$

$$\frac{\mathbf{q}^{n+1}-\mathbf{q}^n}{\Delta t}+\nabla\cdot\left(\frac{\mathbf{q}^n\otimes\mathbf{q}^n}{\rho^n}+p^n\,\mathbb{I}\right)+\frac{1-\varepsilon^2}{\varepsilon^2}\,\nabla p^{n+1}=0, \tag{3.6b}$$

$$\frac{E^{n+1}-E^n}{\Delta t}+\nabla\cdot\left(\frac{E^n+p^n}{\rho^{n+1}}\mathbf{q}^{n+1}\right)=0, \tag{3.6c}$$

with

(3.7)

$$\mathcal{F}_E(U^n)\doteq\begin{pmatrix}\mathbf{q}^n\\ \left(\frac{\mathbf{q}^n\otimes\mathbf{q}^n}{\rho^n}\right)+p^n\,\mathbb{I}\\ 0\end{pmatrix},\quad \mathcal{F}_{SI}(U^n,U^{n+1})\doteq\begin{pmatrix}0\\ \frac{1-\varepsilon^2}{\varepsilon^2}\,p^{n+1}\,\mathbb{I}\\ \frac{E^n+p^n}{\rho^{n+1}}\mathbf{q}^{n+1}\end{pmatrix}.$$

The flow chart based on the semi-implicit scheme is the following:

1. Update ρ^{n+1} from (3.6a).
2. We rewrite (3.6b) as

$$\mathbf{q}^{n+1}=\mathbf{q}^*-\Delta t\frac{1-\varepsilon^2}{\varepsilon^2}\nabla p^{n+1}, \tag{3.8}$$

with $\mathbf{q}^*=\mathbf{q}^n-\Delta t\nabla\cdot(\frac{\mathbf{q}^n\otimes\mathbf{q}^n}{\rho^n}+p^n\mathbb{I})$. We substitute $\mathbf{q}^{n+1}$ into (3.6c) to get

$$E^{n+1}=E^*+\Delta t^2\frac{1-\varepsilon^2}{\varepsilon^2}\nabla\cdot\left(H^n\nabla p^{n+1}\right), \tag{3.9}$$

where $H^n=(E^n+p^n)/\rho^{n+1}$ and $E^*=E^n-\Delta t\nabla\cdot(H^n\mathbf{q}^*)$.

3. Now we replace E^{n+1} by $p^{n+1}/(\gamma-1)+\varepsilon^2|\mathbf{q}|^2/(2\rho^n)$ in (3.9) using (3.3), and with the introduction of (3.4), i.e., $p_2^{n+1}\doteq(p^{n+1}-\bar{p}^n)/\varepsilon^2$ where $p_I=p^{n+1}$ and $\bar{p}^n=\bar{p}_E$, we rewrite (3.9) as

$$\frac{\varepsilon^2}{\gamma-1}p_2^{n+1}-\Delta t^2(1-\varepsilon^2)\nabla\cdot\left(H^n\nabla p_2^{n+1}\right)=E^{**}, \tag{3.10}$$

where $E^{**}=E^*-\bar{p}^n/(\gamma-1)-\varepsilon^2|\mathbf{q}|^2/(2\rho^n)$ is explicitly computed. We obtain an elliptic equation (3.10) for p_2^{n+1}.

4. Finally, we update $\mathbf{q}^{n+1}$ from (3.8), and then E^{n+1} from (3.6c).

Note that if $\varepsilon\geq 1$ the implicit pressure contribution in (3.6b) vanishes, so the momentum $\mathbf{q}^{n+1}$ is evaluated explicitly. With updated ρ^{n+1} and $\mathbf{q}^{n+1}$, E^{n+1} can also be updated in an explicit way from (3.6c).

3.2. High order semi-implicit temporal discretization using IMEX.

3.2.1. High order SI-IMEX-RK scheme for all-Mach number full Euler system. We generalize the first order scheme (3.6) to high order in the framework of IMEX-RK methods. In order to do so, we follow the idea introduced in [4]. We consider an autonomous system of the form

$$U'=\mathcal{H}(U,U),\quad U(t_0)=U_0,$$

where $\mathcal{H} : \mathbb{R}^n \times \mathbb{R}^n \to \mathbb{R}^n$ is a sufficiently regular mapping. We assume an explicit treatment of the first argument of $\mathcal{H}$ (using subscript E), and an implicit treatment to the second argument (using subscript I), i.e.,

$$\begin{cases} U_E' = \mathcal{H}(U_E, U_I), \\ U_I' = \mathcal{H}(U_E, U_I), \end{cases} \tag{3.11}$$

with initial conditions

$$U_E(t_0) = U_0, \quad U_I(t_0) = U_0. \tag{3.12}$$

Then system (3.1) with (3.2) can be rewritten in the form (3.11) where $U \doteq (U_E, U_I)^T$ with $U_E = (\rho_E, \mathbf{q}_E, E_E)^T$, and $U_I = (\rho_I, \mathbf{q}_I, E_I)^T$, and $\mathcal{H}(U_E, U_I) = -\nabla\cdot\mathcal{F}_E - \nabla\cdot\mathcal{F}_{SI}$.

System (3.11) is a particular case of the *partitioned system* [27]. One can apply an IMEX-RK scheme to (3.11), using the corresponding pair of Butcher *tableau* [11],

$$\begin{array}{c|c} \tilde{c} & \tilde{A} \\ \hline & b^T \end{array}, \qquad \begin{array}{c|c} c & A \\ \hline & b^T \end{array}, \tag{3.13}$$

where $\tilde{A} = (\tilde{a}_{ij})$ is an $s \times s$ matrix for an explicit scheme, with $\tilde{a}_{ij} = 0$ for $j \geq i$ and $A = (a_{ij})$ is an $s \times s$ matrix for an implicit scheme. For the implicit part of the methods, we use a diagonally implicit scheme, i.e., $a_{ij} = 0$, for $j > i$, in order to guarantee simplicity and efficiency in solving the algebraic equations corresponding to the implicit part of the discretization. The vectors $\tilde{c} = (\tilde{c}_1, \ldots, \tilde{c}_s)^T$, $\tilde{b} = (\tilde{b}_1, \ldots, \tilde{b}_s)^T$, and $c = (c_1, \ldots, c_s)^T$, $b = (b_1, \ldots, b_s)^T$ complete the characterization of the scheme. The coefficients $\tilde{c}$ and c are given by the usual relation

$$\tilde{c}_i = \sum_{j=1}^{i-1} \tilde{a}_{ij}, \quad c_i = \sum_{j=1}^{i} a_{ij}. \tag{3.14}$$

From now on, it is useful to characterize different IMEX schemes we will consider in what follows according to the structure of the DIRK method. Following [1] we say an IMEX-RK method is of type A if the matrix $A \in \mathbb{R}^{s\times s}$ is invertible, and we say an IMEX-RK method is of type CK if the matrix A can be written as

$$A = \begin{pmatrix} 0 & 0 \\ a & \hat{A} \end{pmatrix}$$

with $a = (a_{21}, \ldots, a_{s1})^T \in \mathbb{R}^{(s-1)}$ and the submatrix $\hat{A} \in \mathbb{R}^{(s-1)\times(s-1)}$ is invertible, or equivalently $a_{ii} \neq 0$, $i = 2, \ldots, s$. In the special case $a = 0$, $b_1 = 0$ the scheme is said to be of type ARS and the DIRK method is reducible to a method using $s - 1$ stages. Later, for the consideration of the AP property, we consider *stiffly accurate* (SA) implicit schemes, i.e., the implicit part of the Butcher table satisfies the condition $b^T = e_s^T A$, with $e_s = (0, \ldots, 0, 1)$ and $c_s = 1$. We will see that SA guarantees that the numerical solution is identical to the last internal stage value of the scheme.

Now an SI-IMEX-RK scheme applied to (3.11) reads

$$U_E^{(i)} = U_E^n + \Delta t \sum_{j=1}^{i-1} \tilde{a}_{ij} \mathcal{H}(U_E^{(j)}, U_I^{(j)}), \quad U_I^{(i)} = U_I^n + \Delta t \sum_{j=1}^{i} a_{ij} \mathcal{H}(U_E^{(j)}, U_I^{(j)}), \tag{3.15a}$$

$$U_E^{n+1} = U_E^n + \Delta t \sum_{i=1}^{s} \tilde{b}_i \mathcal{H}(U_E^{(i)}, U_I^{(i)}), \quad U_I^{n+1} = U_I^n + \Delta t \sum_{i=1}^{s} b_i \mathcal{H}(U_E^{(i)}, U_I^{(i)}). \tag{3.15b}$$

Apparently, by writing in the form (3.11), we increased the computational cost since we double the number of variables. However, the cost is mainly due to the number of function evaluations, which essentially depends on the semi-implicit scheme, because in (3.15) the identical term $\mathcal{H}(U_E^j, U_I^j)$ appears in both explicit and implicit parts. Furthermore, if $\tilde{b}_i = b_i$ for all i, then $U_E^n = U_I^n$ for all $n > 0$ (provided $U_E^0 = U_I^0$) and therefore the duplication of variables is not necessary. Such a property is of particular relevance for designing time discretization schemes which are AP.

We rewrite the scheme (3.15) in the following new form for the convenience of further discussion:

$$U_E^{(i)} = U^n + \Delta t \sum_{j=1}^{i-1} \tilde{a}_{ij} \mathcal{H}(U_E^{(j)}, U_I^{(j)}), \quad U_I^{(i)} = \tilde{U}_I^{(i)} + \Delta t\, a_{ii} \mathcal{H}(U_E^{(i)}, U_I^{(i)}), \tag{3.16}$$

where $\tilde{U}_I^{(i)} = U^n + \Delta t \sum_{j=1}^{i-1} a_{ij} \mathcal{H}(U_E^{(j)}, U_I^{(j)})$. Denoting $U^n = U_E^n = U_I^n$ for all $n > 0$ (due to $\tilde{b}_i = b_i$ for all i), finally we have

$$U^{n+1} = U^n + \Delta t \sum_{i=1}^{s} b_i \mathcal{H}(U_E^{(i)}, U_I^{(i)}). \tag{3.17}$$

Similar to the first order scheme, we split the pressure into explicit (p_E) and implicit (p_I) terms. In order to avoid the nonlinearity in the semi-implicit step we use the following equations of state (3.3), i.e., for the generic stages $i = 1, \dots, s$:

$$E_E^{(i)} = \frac{1}{\gamma - 1} p_E^{(i)} + \varepsilon^2 \frac{|\mathbf{q}_E^{(i)}|^2}{2\rho_E^{(i)}}, \tag{3.18a}$$

$$E_I^{(i)} = \frac{1}{\gamma - 1} p_I^{(i)} + \varepsilon^2 \frac{|\mathbf{q}_E^{(i)}|^2}{2\rho_E^{(i)}}. \tag{3.18b}$$

Remark 3.1. The first order scheme (3.6) is the same as applying the following Butcher table to (3.11):

$$\textbf{Type A I:} \quad \begin{array}{c|c} 0 & 0 \\ \hline & 1 \end{array} \qquad \begin{array}{c|c} 1 & 1 \\ \hline & 1 \end{array}. \tag{3.19}$$

Formally applying the above tableau (3.19) to the partitioned system (3.11), it reads

$$\begin{aligned} U_E^{(1)} &= U^n, \\ U_I^{(1)} &= U^n + \Delta t \mathcal{H}(U_E^{(1)}, U_I^{(1)}), \\ U^{n+1} &= U^n + \Delta t \mathcal{H}(U_E^{(1)}, U_I^{(1)}), \end{aligned}$$

which is the first order scheme (3.6), considering $U_E^{(1)} = U^n$ and $U_I^{(1)} = U^{n+1}$.

Remark 3.2. The authors in [10] proposed a different semi-implicit discretization of the EOS (3.18b) where the kinetic energy in the total energy definition splits into an explicit and an implicit contribution, namely

$$E_I^{(i)} = \frac{1}{\gamma - 1} p_I^{(i)} + \varepsilon^2 \frac{|(\mathbf{q}_E^{(i)})^T \mathbf{q}_I^{(i)}|}{2\rho_I^{(i)}}. \tag{3.20}$$

We performed numerical tests to compare such semi-implicit treatment of the kinetic energy (3.20) with (3.18b). It is found numerically that such semi-implicit treatment

(3.20) may produce slightly better error in some test cases. Overall comparable performances are observed. In order to save space, we decided not to report these results in this paper.

3.2.2. Construction of an IMEX-RK scheme. Next, we construct an IMEX-RK Butcher tableau for semi-implicit discretization of the all-Mach full Euler system. The construction is based on the following considerations for accuracy and for handling non-well-prepared initial data.

1. We require that the implicit part of the IMEX-RK scheme is SA. With such an assumption, one can derive the AP and AA properties of the scheme as discussed in section 4. Note that if the implicit part of the scheme is A-stable, SA is a sufficient condition to make it L-stable; see [27].
2. The invertibility of the implicit matrix A of the SI-IMEX-RK scheme is important to handle non-well-prepared initial conditions and for proper initialization of the hydrodynamic pressure. In particular, $a_{11} \neq 0$ for IMEX-RK schemes of type A. This is critical to solve the pressure wave equation (3.10). If $a_{11} = 0$ (e.g., in an IMEX scheme of type ARS), then we can not have the pressure wave equation, hence no proper value of $p_{I,2}$ (e.g., see (3.29)) at the first IMEX stage. For further related discussions and analysis, we refer the reader to the papers [40, 7, 6]. Thus, we construct IMEX-RK of type A for the time discretization.
3. To synchronize U_E and U_I, the weights for the final stage of the double tableaus should be the same, i.e., $\tilde{b}_i = b_i$, $i = 1, \ldots, s$. That is, we keep only one set of numerical solution in the process of updating [4]. Alternatively, we can select a different vector of weights for the $U_E(t)$, say, $\tilde{b}_i \neq b_i$, which will provide a lower/higher order approximation of the solution for $U_E(t)$; this can be used to implement a procedure of automatic time step control [26].
4. In order to simplify order conditions, given the equations of state used in the semi-implicit step (3.18), we impose that $c_i = \tilde{c}_i$, $i = 2, \ldots, s$. Note that if matrix A is invertible we have $c_1 \neq \tilde{c}_1 = 0$ [40].

Based on the above considerations, we design a high-order IMEX scheme with matrix A invertible, which is SA and satisfies $c_i = \tilde{c}_i$ for $i = 2, \ldots, s$. We impose the conditions required for a third order scheme [40] and obtain the following double Butcher tableau:

Explicit :

0	0	0	0	0
γ	γ	0	0	0
0.717933260754	0.435866521508	0.282066739245	0	0
1	−0.733534082748750	2.150527381100	−0.416993298352	0
0	0	1.208496649176	−0.644363170684	γ

,

(3.21)

Implicit :

γ	γ	0	0	0
γ	0	γ	0	0
0.717933260754	0	0.282066739245	γ	0
1	0	1.208496649176	−0.644363170684	γ
	0	1.208496649176	−0.644363170684	γ

,

with $\gamma = 0.435866521508$. We call it SI-IMEX(4,4,3), the triplet (s, σ, p) characterizing the number of stages of the implicit scheme ($s = 4$), the number of stages of the explicit scheme ($\sigma = 4$) and the order of the scheme ($p = 3$). A corresponding second order scheme, which we call SI-IMEX(3,3,2), is given as

(3.22)

Explicit :

$$\begin{array}{c|cccc} 0 & 0 & 0 & 0 \\ \gamma & \gamma & 0 & 0 \\ 1 & \delta & 1-\delta & 0 \\ \hline 0 & 0 & 1-\gamma & \gamma \end{array},$$

Implicit :

$$\begin{array}{c|cccc} \gamma & \gamma & 0 & 0 \\ \gamma & 0 & \gamma & 0 \\ 1 & 0 & 1-\gamma & \gamma \\ \hline 0 & 0 & 1-\gamma & \gamma \end{array},$$

where $\gamma = 1 - \sqrt{2}/2$ and $\delta = -2\sqrt{2}/3$.

3.3. High order spatial discretization for all-Mach fluid flows. Below we describe our spatial discretization strategies that incorporate a WENO mechanism to capture shocks in the compressible regime and produce a high order incompressible solver for the flow in the zero Mach limit. One major difficulty, hence the new ingredient in the scheme design, in extending the high order AP scheme for the isentropic Euler system [8] to the full Euler system is about the pressure. In the isentropic case, the pressure is an explicit function of ρ, whereas in the full Euler case the pressure comes from the EOS involving all conserved variables. As such, we split the pressure into the part involving p_E obtained from the EOS (3.18a) and the part $p_{I,2}$ obtained by formulating an elliptic equation from a semi-implicit solver of the system. In this process, the spatial discretization in the scheme formulation becomes critical for its robustness. There are several ingredients in our spatial discretization that differentiate our approach from the existing ones in the literature. First, we carefully apply the WENO procedure for spatial reconstructions of fluxes for the full Euler system which is a nontrivial generalization from the isentropic one [8]. In particular, we propose to apply the fifth order characteristicwise WENO procedure to $\mathcal{F}_E$ (in (3.2)) of the full Euler system so that in the compressible regime oscillations could be best controlled, and to apply a componentwise WENO procedure for the flux functions of $\mathcal{F}_{SI}$ (in (3.2)). We found that such a choice is optimal in compromising the need from both compressible and incompressible fluid solvers. The characteristicwise WENO turns out to be important for the compressible Euler system, as shown in the numerical section. Second, following the strategy in our previous work [8], we apply a compact high order spatial discretization to second order derivatives terms in (3.28). This is discussed in section 3.3.2.

3.3.1. WENO spatial discretization. Without loss of generality, we describe our algorithms in a two-dimensional (2D) setting. Let

$$U = (\rho, \rho u, \rho v, E)^T,$$
$$\nabla \cdot \mathcal{F}_E = \partial_x \mathcal{F}_E^x + \partial_y \mathcal{F}_E^y, \quad \nabla \cdot \mathcal{F}_{SI} = \partial_x \mathcal{F}_{SI}^x + \partial_y \mathcal{F}_{SI}^y$$

with flux functions in x and y directions

$$\mathcal{F}_E^x = (\rho u, \rho u^2 + p, \rho uv, 0)^T, \quad \mathcal{F}_E^y = (\rho v, \rho uv, \rho v^2 + p, 0)^T,$$
$$\mathcal{F}_{SI}^x = \left(0, \frac{1-\varepsilon^2}{\varepsilon^2} p, 0, \frac{E+p}{\rho}(\rho u)\right)^T, \quad \mathcal{F}_{SI}^y = \left(0, 0, \frac{1-\varepsilon^2}{\varepsilon^2} p, \frac{E+p}{\rho}(\rho v)\right)^T.$$

We consider a rectangular domain discretized by a uniform Cartesian grid, with mesh size $\Delta x = \Delta y$, and grid points (x_i, y_j), $i = 1, \ldots, N_x$, $j = 1, \ldots, N_y$, located at cell

centers. We use the subscript $\cdot_{i,j}$ to denote the solution point values at (x_i, y_j) and use $\cdot_{i\pm1/2,j}$ and $\cdot_{i,j\pm1/2}$ for the reconstructed numerical fluxes in approximating x- and y- derivatives, respectively.

Below we first present two types of WENO spatial discretizations, i.e., a characteristicwise WENO and a componentwise WENO, for explicit and semi-implicit parts as specified in (3.2), respectively.

1. *Characteristicwise WENO ∇_{CW} with Lax–Friedrichs splitting for discretizing $\nabla\cdot\mathcal{F}_E$.* For compressible hyperbolic systems with shocks, WENO reconstructions in the componentwise fashion may still lead to oscillations and a local characteristic decomposition will be needed [42]. We let $\mathcal{F}^x_{E,i,j}$ be the flux function at each grid point (x_i, y_j). To approximate the $\partial_x\mathcal{F}^x_E|_{x_i,y_j}$, we fix a j-index and perform a global Lax–Friedrichs splitting for the flux terms, i.e.,
$$\mathcal{F}^x_{E,i,j} = \mathcal{F}^{x,+}_{E,i,j} + \mathcal{F}^{x,-}_{E,i,j} \quad \forall i$$
with
(3.23)
$$\mathcal{F}^{x,\pm}_{E,i,j} = \frac{1}{2}(\mathcal{F}^x_{E,i,j} \pm \Lambda U_{E,i,j}), \quad \Lambda = \max_{u,v}\left\{|u|+|v|+\min\left\{1,\frac{1}{\varepsilon}\right\} c_s\right\}$$
with $c_s = \sqrt{\gamma p/\rho}$ being the sound speed multipled by ε, and the max is taken over appropriate range of u, v. Notice that such a choice of Λ is the same as in our previous work [8]. We then project $\{\mathcal{F}^{x,\pm}_{E,i,j}\}_{i=1}^{N_x}$ to local characteristics directions for the full Euler system in the compressible regime (corresponding to $\varepsilon = 1$), perform WENO reconstruction of fluxes there, and then project the reconstructed fluxes back, to obtain the flux terms as
$$\hat{\mathcal{F}}^x_{E,i+\frac{1}{2},j} = \hat{\mathcal{F}}^{x,+}_{E,i+\frac{1}{2},j} + \hat{\mathcal{F}}^{x,-}_{E,i+\frac{1}{2},j}.$$
Then
$$\partial_x\mathcal{F}^x_E|_{x_i,y_j} \approx \frac{1}{\Delta x}\left(\hat{\mathcal{F}}^x_{E,i+\frac{1}{2},j} - \hat{\mathcal{F}}^x_{E,i-\frac{1}{2},j}\right).$$
A similar procedure could be performed to approximate spatial derivatives in the y-direction. We introduce the notation of ∇_{CW} for the characteristicwise WENO spatial discretization of $\mathcal{F}_E$.
2. *A componentwise WENO ∇_W with Lax–Friedrichs flux splitting for discretizing $\nabla\cdot\mathcal{F}_{SI}$.* We apply a componentwise WENO reconstruction of fluxes for discretizing $\nabla\cdot\mathcal{F}_{SI}$ denoted as $\nabla_W\cdot\mathcal{F}_{SI}$. In particular, a Lax–Friedrichs flux splitting, followed by a componentwise WENO reconstruction, is performed to obtain the numerical fluxes.

3.3.2. Flowchart and compact discretization of second order derivatives. With the introduction of characteristicwise and componentwise WENO ∇_{CW} and ∇_W, we summarize the flow chart of the SI-IMEX-RK time discretization (3.16)–(3.17), coupled with WENO spatial discretization, for solving the all-Mach full Euler system. In this process, a compact high order discretization for second order spatial derivatives in (3.28) is applied.

1. Starting from U^n at time t^n, we first compute $U_E^{(i)}$ from (3.16),

$$\rho_E^{(i)} = \rho^n - \Delta t \sum_{j=1}^{i-1} \tilde{a}_{ij} \nabla_{CW} \cdot \mathbf{q}_E^{(j)}, \tag{3.24a}$$

(3.24b)

$$\mathbf{q}_E^{(i)} = \mathbf{q}^n - \Delta t \sum_{j=1}^{i-1} \tilde{a}_{ij} \left(\nabla_{CW} \cdot \left(\frac{\mathbf{q}_E^{(j)} \otimes \mathbf{q}_E^{(j)}}{\rho_E^{(j)}} + p_E^{(j)} \mathbb{I} \right) + (1-\varepsilon^2) \frac{\nabla_W p_I^{(j)}}{\varepsilon^2} \right),$$

$$E_E^{(i)} = E^n - \Delta t \sum_{j=1}^{i-1} \tilde{a}_{ij} \nabla_W \cdot \left(\bar{H}^{(j)} \mathbf{q}_I^{(j)} \right). \tag{3.24c}$$

2. We compute $\tilde{U}^{(i)}$ in (3.16).

$$\tilde{\rho}^{(i)} = \rho^n - \Delta t \sum_{j=1}^{i-1} a_{ij} \nabla_{CW} \cdot \mathbf{q}_E^{(j)}, \tag{3.25a}$$

(3.25b)

$$\tilde{\mathbf{q}}^{(i)} = \mathbf{q}^n - \Delta t \sum_{j=1}^{i-1} a_{ij} \left(\nabla_{CW} \cdot \left(\frac{\mathbf{q}_E^{(j)} \otimes \mathbf{q}_E^{(j)}}{\rho_E^{(j)}} + p_E^{(j)} \mathbb{I} \right) + (1-\varepsilon^2) \frac{\nabla_W p_I^{(j)}}{\varepsilon^2} \right),$$

$$\tilde{E}^{(i)} = E^n - \Delta t \sum_{j=1}^{i-1} a_{ij} \nabla_W \cdot \left(\bar{H}^{(j)} \mathbf{q}_I^{(j)} \right) \tag{3.25c}$$

with $\bar{H}^{(j)} = (E_E^{(j)} + p_E^{(j)})/\rho_I^{(j)}$.

3. Solve $U_I^{(i)}$ from (3.16).
   (a) In components, $U_I^{(i)}$ satisfies

$$\rho_I^{(i)} = \tilde{\rho}^{(i)} - \Delta t \, a_{ii} \nabla_{CW} \cdot \mathbf{q}_E^{(i)}, \tag{3.26a}$$

$$\mathbf{q}_I^{(i)} = \tilde{\tilde{\mathbf{q}}}^{(i)} - \Delta t \, a_{ii} \left(\frac{1-\varepsilon^2}{\varepsilon^2} \nabla p_I^{(i)} \right), \tag{3.26b}$$

$$E_I^{(i)} = \tilde{E}^{(i)} - \Delta t a_{ii} \nabla \cdot (\bar{H}_i \mathbf{q}_I^{(i)}), \tag{3.26c}$$

   where

$$\tilde{\tilde{\mathbf{q}}}^{(i)} = \tilde{\mathbf{q}}^{(i)} - \Delta t \, a_{ii} \left(\nabla_{CW} \cdot \left(\frac{\mathbf{q}_E^{(i)} \otimes \mathbf{q}_E^{(i)}}{\rho_E^{(i)}} + p_E^{(i)} \mathbb{I} \right) \right). \tag{3.27}$$

   (b) To solve the system (3.26), we substitute $\mathbf{q}_I^{(i)}$ of (3.26b) into (3.26c) and obtain

$$E_I^{(i)} = E_I^{**} + (1-\varepsilon^2) \Delta t^2 \, a_{ii}^2 \nabla \left(\bar{H}^{(i)} \left(\frac{\nabla p_I^{(i)}}{\varepsilon^2} \right) \right) \tag{3.28}$$

   with $E_I^{(i)}$ following the EOS (3.18b) and $E_I^{**} = \tilde{E}^{(i)} - \Delta t \, a_{ii} \nabla_W \cdot (\bar{H}^{(i)} \tilde{\tilde{\mathbf{q}}}^{(i)})$. (3.28) is an implicit equation about $p_I^{(i)}$. By the introduction of pressure perturbation $p_{I,2}^{(i)}$ in (3.4), we solve $p_{I,2}^{(i)}$ from

$$\frac{\varepsilon^2}{\gamma - 1} p_{I,2}^{(i)} = E_I^{***} + (1-\varepsilon^2) \Delta t^2 \, a_{ii}^2 \nabla \left(\bar{H}^{(i)} \left(\nabla p_{I,2}^{(i)} \right) \right), \tag{3.29}$$

where $E_I^{***} = E_I^{**} - \bar{p}_E/(\gamma-1) - \varepsilon^2|\mathbf{q}_E^{(i)}|^2/(2\rho_E^{(i)})$. Notice that in the process of substitution to obtain (3.28) or (3.29), the gradient and the divergence operators are kept continuous, obtaining the second order operator $\nabla(\bar{H}^{(i)}\nabla p_{I,2}^{(i)})$. The second order spatial derivative is then discretized by a compact discretization as proposed in [8].

(c) With $p_{I,2}^{(i)}$ solved from (3.29), we update $\mathbf{q}_I^{(i)}$ from

$$\mathbf{q}_I^{(i)} = \tilde{\tilde{\mathbf{q}}}^{(i)} - \Delta t\, a_{ii}\left(1-\varepsilon^2\right)\nabla_W p_{I,2}^{(i)} \tag{3.30}$$

and successively update $E_I^{(i)}$ from

$$E_I^{(i)} = \tilde{E}^{(i)} - \Delta t a_{ii}\nabla_W \cdot (\bar{H}_i \mathbf{q}_I^{(i)}). \tag{3.31}$$

4. Finally, update the numerical solution $U^{n+1} = U_I^{(s)}$ with the assumption on the SA property of IMEX-RK schemes.

This completes the description of the high order SI-IMEX-RK time discretization to the all-Mach full Euler equations.

4. Asymptotic preserving and asymptotically accurate properties.

4.1. AP property. In this section we prove the AP property of scheme (3.6). In particular, we prove that its limiting scheme is consistent with the continuous limit model (2.6) at $\varepsilon = 0$. We focus on the AP analysis on time discretizations, while keeping the space continuous. We assume that the data at time t^n are well-prepared in the sense of (2.3), i.e., $p^n(\mathbf{x}) := p(t^n, \mathbf{x})$ and $\mathbf{u}^n(\mathbf{x}) := \mathbf{u}(t^n, \mathbf{x})$ admit the decomposition:

$$p^n(\mathbf{x}) = p_0^n + \varepsilon^2 p_2^n(\mathbf{x}), \quad \mathbf{u}^n(\mathbf{x}) = \mathbf{u}_0^n(\mathbf{x}) + \mathcal{O}(\varepsilon), \tag{4.1}$$

where $p_0^n = (\gamma-1)E_0^n$ is a constant and $\nabla \cdot \mathbf{u}_0^n(\mathbf{x}) = 0$.

Then we consider an expansion in powers of ε of the form (2.3) and we plug it into the semidiscrete scheme (3.6). Equating to zero the $\mathcal{O}(\varepsilon^{-2})$ term we have

$$\nabla p_0^{n+1} = 0. \tag{4.2}$$

Equating to zero the $\mathcal{O}(\varepsilon^0)$ terms, we have

$$\frac{\rho_0^{n+1} - \rho_0^n}{\Delta t} + \nabla \cdot (\rho_0^n \mathbf{u}_0^n) = 0, \tag{4.3a}$$

$$\frac{\rho_0^{n+1}\mathbf{u}_0^{n+1} - \rho_0^n \mathbf{u}_0^n}{\Delta t} + \nabla \cdot (\rho_0^n \mathbf{u}_0^n \otimes \mathbf{u}_0^n) + \nabla p_2^{n+1} = 0, \tag{4.3b}$$

$$E_0^{n+1} = p_0^{n+1}/(\gamma-1), \tag{4.3c}$$

$$\frac{E_0^{n+1} - E_0^n}{\Delta t} + \nabla \cdot \left(\bar{H}_0^n(\rho_0^{n+1}\mathbf{u}_0^{n+1})\right) = 0 \tag{4.3d}$$

with

$$\bar{H}_0^n = \frac{p_0^n + E_0^n}{\rho_0^{n+1}} = \frac{\gamma}{\gamma-1}\frac{p_0^n}{\rho_0^{n+1}}. \tag{4.4}$$

By (4.3c) and (4.4), (4.3d) is equivalent to

$$\frac{p_0^{n+1} - p_0^n}{\Delta t} + \gamma\, p_0^n\, \nabla \cdot \mathbf{u}_0^{n+1} = 0. \tag{4.5}$$

Note that (4.5) is the time discretization of the limiting equation for the pressure (2.5).

From (4.2), it follows that p_0^{n+1} is independent of space. Now, as in the continuous case, integrating (4.5) over a spatial domain Ω and assuming some boundary conditions (for example, no-slip or periodic), we get $p_0^{n+1} = p_0^n$, i.e., p_0^{n+1} is also independent of time. Using this in (4.5), we obtain the divergence-free condition for the velocity $\nabla \cdot \mathbf{u}_0^{n+1} = 0$.

This yields the following theorem.

THEOREM 4.1. *The time-discrete scheme* (4.3) *is AP in the sense that at the leading order asymptotic expansion,* (4.3a), (4.3b) *with* p_0^{n+1} *constant and* $\nabla \cdot \mathbf{u}_0^{n+1} = 0$ *are a consistent approximation of the incompressible Euler equations* (2.6).

Another noticeable feature of the time-discrete scheme (4.3) is that we can obtain a time-discrete version for the elliptic equation (2.8). We get it by applying the divergence operator to the momentum equation (4.3b), after some algebraic manipulations, and making use of the density equation (4.3a). The resulting relation is

$$\nabla \cdot \left(\frac{\rho_0^n}{\rho_0^{n+1}} (\mathbf{u}_0^n \cdot \nabla) \mathbf{u}_0^n \right) = -\nabla \cdot \left(\frac{1}{\rho_0^{n+1}} \nabla p_2^{n+1} \right),$$

which is a consistent discretization of (2.8) because $\rho_0^n / \rho_0^{n+1} = 1 + \mathcal{O}(\Delta t)$.

Note that once it is established that $\nabla \cdot \mathbf{u}_0^{n+1} = 0$, from the first equation of (2.4) it follows that if the initial density ρ_0^0 is constant, then it remains constant for any later time.

Remark 4.2. Note that in [16] the authors proposed a scheme similar to (3.6), but with a slight difference in the explicit treatment of the density in the energy equation, i.e.,

$$\frac{E^{n+1} - E^n}{\Delta t} + \nabla \cdot \left(\frac{E^n + p^n}{\rho^n} \mathbf{q}^{n+1} \right) = 0.$$

Their scheme is AP, i.e., it is consistent with the limiting equations (2.4) in the incompressible regime. However, as $\varepsilon \to 0$, they prove that the divergence-free condition on the velocity is explicitly satisfied up to the order of the approximation with the CFL condition independent of the Mach number ε, i.e., $\nabla \cdot \mathbf{u}_0^{n+1} = \mathcal{O}(\Delta t)$ (see the proposition in section 4.2 in [16]). In our case, instead, scheme (3.6) has the correct discrete divergence-free condition for the leading order velocity $\mathbf{u}_0^{n+1}$, i.e., $\nabla \cdot \mathbf{u}_0^{n+1} = 0$.

4.2. AA property. The AP property guarantees only the consistency of the scheme, but in general the AP property does not guarantee the high order accuracy of IMEX schemes in the limit for $\varepsilon \ll 1$, i.e., as $\varepsilon \to 0$ the order of accuracy may degrade. In what follows, we first formally state the definition of the AA property, and then we recognize that the SA condition is crucial to guarantee the AA property of our SI-IMEX-RK scheme. Similarly as the AP property, here we focus on the AA analysis on time discretizations, while keeping space continuous.

DEFINITION 4.3. *A semi-implicit temporal discretization for the Euler system* (2.1) *is said to be AA, if it maintains its order of temporal accuracy for the limiting system* (2.4) *when* $\varepsilon \to 0$.

PROPOSITION 4.4. *Consider an SI-IMEX-RK scheme* (3.16)–(3.17) *of order r applied to system* (2.1) *in a bounded domain* $\Omega \subset \mathbb{R}$ *with zero Neumann condition.*

Assume that the implicit part of the IMEX-RK scheme is SA and that the initial conditions $(\rho^0(\mathbf{x}), \rho^0(\mathbf{x})\mathbf{u}^0(\mathbf{x}), p^0)^T$ *are well-prepared in the form of* (2.9)*. Let us denote by* $(\rho^1(\mathbf{x};\varepsilon),\ \rho^1(\mathbf{x};\varepsilon)\mathbf{u}^1(\mathbf{x};\varepsilon),\ p^1(\mathbf{x};\varepsilon))^T$ *the numerical solution after one time step. Then we have*

$$\lim_{\varepsilon\to 0} p^1(\mathbf{x};\varepsilon) = p_*, \quad \lim_{\varepsilon\to 0} \nabla\cdot\mathbf{u}^1(\mathbf{x};\varepsilon) = 0 \tag{4.6}$$

with p_* *a constant.*

Furthermore, let $\mathbf{V}_{inc}(\mathbf{x},t) = (\rho_{inc}(\mathbf{x},t), \rho_{inc}(\mathbf{x},t)\mathbf{u}_{inc}(\mathbf{x},t), p_{inc}(\mathbf{x},t))^T$ *be the exact solution of the incompressible Euler equations* (2.6) *with the same initial data. Then one has the one-step error estimate*

$$\lim_{\varepsilon\to 0} \mathbf{V}^1(\mathbf{x};\varepsilon) = \mathbf{V}_{inc}(\mathbf{x},\Delta t) + \mathcal{O}(\Delta t^{r+1}), \tag{4.7}$$

i.e., the scheme is AA.

Proof. We consider the first step from $t^0 = 0$ to $t^1 = \Delta t$ for the SI-IMEX-RK scheme (3.16)–(3.17) of order r applied to system (2.1) with well-prepared initial data (4.1),

$$\rho^0(\mathbf{x}) = \rho^0_{inc} + \varepsilon^2\,\rho^0_2(\mathbf{x}), \quad p^0(\mathbf{x}) = p_* + \varepsilon^2\,p^0_2(\mathbf{x}), \quad \mathbf{u}^0(\mathbf{x}) = \mathbf{u}^0_{inc} + \mathcal{O}(\varepsilon),$$

where $\rho^0_{inc} := \rho_{inc}(\mathbf{x},0)$, $\mathbf{u}^0_{inc} := \mathbf{u}_{inc}(\mathbf{x},0)$, and by the well-prepared assumption we have $p_{inc}(\mathbf{x},0) := p_*$ constant independent of time and space, and $\nabla\cdot\mathbf{u}^0_{inc} = 0$.

Now we consider a formal ε-expansion of the quantities $U^{(i)}_I = (\rho^{(i)}_I, \mathbf{q}^{(i)}_I, E^{(i)}_I)^T$, and $U^{(i)}_E = (\rho^{(i)}_E, \mathbf{q}^{(i)}_E, E^{(i)}_E)^T$ with $\mathbf{q}^{(i)}_I = \rho^{(i)}_I\mathbf{u}^{(i)}_I$ and $\mathbf{q}^{(i)}_E = \rho^{(i)}_E\mathbf{u}^{(i)}_E$, as an example for the density and pressure:

$$\begin{aligned} &\rho^{(i)}_I = \rho^{(i)}_{0,I} + \varepsilon^2\,\rho^{(i)}_{2,I} + \dots, \qquad \rho^{(i)}_E = \rho^{(i)}_{0,E} + \varepsilon^2\,\rho^{(i)}_{2,E} + \dots, \\ &p^{(i)}_I = p^{(i)}_{0,I} + \varepsilon^2\,p^{(i)}_{2,I} + \dots, \qquad p^{(i)}_E = p^{(i)}_{0,E} + \varepsilon^2\,p^{(i)}_{2,E} + \dots. \end{aligned} \tag{4.8}$$

In order to prove the theorem, we use the mathematical induction.

- *Asymptotic accuracy for the internal stages* $i = 1,\dots,s$.
  Case $i = 1$ leads to the same AP analysis for the scheme (3.6) with Δt replaced by $a_{11}\Delta t$. To prove the result for $i > 1$ onward, we make use of the induction hypothesis, assuming the property holds for $j \le i-1$, and prove that it holds for $j = i$. Then for $j = 1,\dots,i-1$ we have

  $$p^{(j)}_{0,E} = p_*, \quad E^{(j)}_{0,E} = \frac{p_*}{\gamma-1}, \quad \nabla\cdot\mathbf{u}^{(j)}_{0,I} = 0. \tag{4.9}$$

  Now we insert the expansions (4.8) into the explicit step in (3.16), and we get for the energy equation

  $$E^{(i)}_{0,E} = E^0_{inc} - \Delta t\sum_{j=1}^{i-1}\tilde a_{ij}\nabla\cdot\left(\bar H^{(j)}_0\mathbf{q}^{(j)}_{0,I}\right) \tag{4.10}$$

  with $E^0_{inc} = p_*/(\gamma-1)$ and for $j = 1,\dots,i-1$,

  $$\bar H^{(j)}_0 = \frac{E^{(j)}_{0,E} + p^{(j)}_{0,E}}{\rho^{(j)}_{0,I}} = \frac{\gamma}{\gamma-1}\frac{p_*}{\rho^{(j)}_{0,I}}. \tag{4.11}$$

Now by (4.9), (4.11), and $E_{0,E}^{(i)} = p_{0,E}^{(i)}/(\gamma-1)$, from (4.10) we obtain

$$p_{0,E}^{(i)} = p_* - \Delta t\,\gamma\, p_* \sum_{j=1}^{i-1} \tilde{a}_{ij} \nabla \cdot \mathbf{u}_{0,I}^{(j)} = p_*, \tag{4.12}$$

that is, $p_{0,E}^{(i)} = p_*$ is constant. Then $E_{0,E}^{(i)} = p_*/(\gamma-1)$ is also constant for the stage i.
From (3.16), to $\mathcal{O}(1)$ we obtain for the density and momentum equations

$$\rho_{0,E}^{(i)} = \rho_{inc}^0 - \Delta t \sum_{j=1}^{i-1} \tilde{a}_{ij} \nabla \cdot \mathbf{q}_{0,E}^{(j)} \tag{4.13}$$

and

$$\mathbf{q}_{0,E}^{(i)} = \mathbf{q}_{inc}^0 - \Delta t \sum_{j=1}^{i-1} \tilde{a}_{ij} \left(\nabla \cdot \left(\rho_{0,E}^{(j)}\, \mathbf{u}_{0,E}^{(j)} \otimes \mathbf{u}_{0,E}^{(j)} \right) + \nabla p_{2,I}^{(j)} \right) \tag{4.14}$$

with $\mathbf{q}_{inc}^0 = (\rho \mathbf{u})_{inc}^0$ and $\nabla p_{0,E}^{(j)} = 0$ for $j = 1, \ldots, i-1$.
Similarly, inserting expansions (4.8) into (3.25b), up to $\mathcal{O}(1)$ we get for the intermediate explicit step $\tilde{U}_0^{(i)}$ in (3.16)

$$\tilde{\mathbf{q}}_0^{(i)} = \mathbf{q}_{inc}^0 - \Delta t \sum_{j=1}^{i-1} a_{ij} \left(\nabla \cdot \left(\rho_{0,E}^{(j)} \mathbf{u}_{0,E}^{(j)} \otimes \mathbf{u}_{0,E}^{(j)} \right) + \nabla p_{2,I}^{(j)} \right), \tag{4.15}$$

where from (3.4) and (4.9), it follows $\nabla \bar{p}_E^{(j)} = 0$ for $j = 1, \ldots, i-1$. Furthermore, from (3.25a) we have

$$\tilde{\rho}_0^{(i)} = \rho_{inc}^0 - \Delta t \sum_{j=1}^{i-1} a_{ij} \nabla \cdot \mathbf{q}_{0,E}^{(j)}, \tag{4.16}$$

and using (4.11), we get

$$\tilde{E}_0^{(i)} = E_{inc}^0 - \Delta t \sum_{j=1}^{i-1} a_{ij} \nabla \cdot (\bar{H}_0^{(j)} \mathbf{q}_{0,I}^{(j)}) = \frac{p_*}{\gamma-1} - \frac{\gamma\, p_*}{\gamma-1} \Delta t \sum_{j=1}^{i-1} a_{ij} \nabla \cdot \mathbf{u}_{0,I}^{(j)}. \tag{4.17}$$

Thus, by (4.9) we get from (4.17)

$$\tilde{E}_0^{(i)} = \frac{p_*}{\gamma-1}. \tag{4.18}$$

Now from (3.15b) and (4.18), it follows for the energy equation

$$E_{0,I}^{(i)} = \tilde{E}_0^{(i)} - \Delta t\, a_{ii} \nabla \cdot (\bar{H}_0^{(i)} \mathbf{q}_{0,I}^{(i)}) = \frac{p_*}{\gamma-1} - \Delta t\, a_{ii} \frac{\gamma\, p_*}{\gamma-1} \nabla \cdot \mathbf{u}_{0,I}^{(i)}.$$

Considering the EOS (3.18b) to zeroth order in ε, we get $E_{0,I}^{(i)} = p_{0,I}^{(i)}/(\gamma-1)$, and we obtain for the pressure

$$p_{0,I}^{(i)} = p_* + \Delta t\, \gamma\, p_*\, a_{ii} \nabla \cdot \mathbf{u}_{0,I}^{(i)}.$$

Integrating it over spatial bounded domain Ω, and assuming some boundary conditions (for example, no-slip or periodic,) we first obtain $p_{0,I}^{(i)} = p_*$ and by this we get $\nabla \cdot \mathbf{u}_{0,I}^{(i)} = 0$ at the stage i.
Finally, from (3.15b), considering (4.15) and (4.16), we get for the density and momentum,

$$\rho_{0,I}^{(i)} = \rho_{inc}^0 - \Delta t \sum_{j=1}^{i} a_{ij} \nabla \cdot \mathbf{q}_{0,E}^{(j)}, \tag{4.19a}$$

$$\mathbf{q}_{0,I}^{(i)} = \mathbf{q}_{inc}^0 - \Delta t \sum_{j=1}^{i} a_{ij} \left(\nabla \cdot \left(\rho_{0,E}^{(j)} \mathbf{u}_{0,E}^{(j)} \otimes \mathbf{u}_{0,E}^{(j)} \right) + \nabla p_{2,I}^{(j)} \right), \tag{4.19b}$$

where from (3.4) and $p_{0,E}^{(i)} = p_*$ it follows in the equation of the momentum $\nabla \bar{p}_E^{(i)} = 0$ for i.
Then (4.13), (4.14), 4.19a), (4.19b), with constant limiting pressure, i.e., $p_{0,E}^{(i)} = p_{0,I}^{(i)} = p_*$, and the divergence-free leading order velocity, i.e., $\nabla \cdot \mathbf{u}_{0,I}^{(i)} = 0$, provide the discretization of system (2.6) for the internal stage i of the SI-IMEX-RK scheme. This shows that in the limit $\varepsilon \to 0$, the scheme becomes the same SI-IMEX-RK time-discrete scheme for the incompressible Euler equations (2.6).

- *Asymtotic accuracy for the numerical solution.*
  Assuming that the SI-IMEX-RK scheme (3.13) is SA, then the numerical solution coincides with the last internal stage s, and then by setting $i = s$, we get

$$p_0^1 = p_{0,I}^{(s)} = p_*, \quad \nabla \cdot \mathbf{u}_0^1 = \nabla \cdot \mathbf{u}_{0,I}^{(s)} = 0, \tag{4.20}$$

  i.e., we have (4.6).
  Now if we denote by $\mathbf{V}_{inc}(\mathbf{x}, t) = (\rho_{inc}(\mathbf{x}, t), \rho_{inc}(\mathbf{x}, t)\mathbf{u}_{inc}(\mathbf{x}, t), p_{inc}(\mathbf{x}, t))^T$ the exact solutions of (2.6), with initial data $\mathbf{V}_{inc}(\mathbf{x}, 0) = (\rho^0(\mathbf{x}), \rho^0(\mathbf{x})\mathbf{u}^0(\mathbf{x}), p^0)^T$, from (4.13), (4.14), (4.19b), and (4.19a) with (4.20), one gets in the limit case $\varepsilon = 0$ a SI-IMEX-RK scheme of order r for the numerical solutions of (2.6), that is, the SI-IMEX-RK scheme (3.16)–(3.17) of order r is AA, and the conclusion (4.7) is obtained. ∎

5. Numerical tests. Through an extensive set of 1D and 2D numerical tests, we will show that our scheme is uniformly stable and effective and can capture the correct asymptotic limit. We use the third order SI-IMEX(4,4,3) scheme in time (3.21), fourth order compact central difference discretization for second order derivatives in the elliptic equation (3.28), and fifth order finite difference WENO reconstruction in space for both ∇_W and ∇_{CW} in section 3.3. Overall the scheme is fourth order in space and third order in time, denoted as "S4T3." On the other hand, an "S2T2" scheme refers to using a second order total variation bounded reconstruction with the parameter $M = 1$ instead of a fifth order WENO reconstruction in the S4T3 scheme, and a second order SI-IMEX(3,3,2) scheme in time (3.22). Reference solutions are computed by a fifth order finite difference WENO scheme with third order explicit RK time discretization [42], denoted as "WENO5RK3." For simplicity, we all take $\gamma = 1.4$ with an ideal EOS. The time step is $\Delta t = \mathrm{CFL}\, \Delta x / \Lambda$, where $\Lambda = \max_x (|u| + \min(1/\varepsilon, 1)\, c_s)$ in one dimension and $\Lambda = \max_{x,y} (|u| + |v| + \min(1/\varepsilon, 1)\, c_s)$ in two dimensions, respectively. $c_s = \sqrt{\gamma p/\rho}$ is the scaled sound speed. We take $\mathrm{CFL} = 0.25$ for all tests.

Example 5.1 (two colliding acoustic pulses [34, 39]). This problem is defined on the domain $-L \le x \le L = 2/\varepsilon$ with periodic boundary condition and initial data

$$\begin{cases} \rho(x,0) = \rho_0 + \frac{1}{2}\varepsilon\rho_1\left(1-\cos\left(2\pi x/L\right)\right), & \rho_0 = 0.955, \quad \rho_1 = 2.0; \\ u(x,0) = \frac{1}{2}u_0\,\mathrm{sign}(x)\left(1-\cos\left(2\pi x/L\right)\right), & u_0 = 2\sqrt{\gamma}; \\ p(x,0) = p_0 + \frac{1}{2}\varepsilon p_1\left(1-\cos\left(2\pi x/L\right)\right), & p_0 = 1.0, \quad p_1 = 2\gamma. \end{cases} \tag{5.1}$$

We first test the order of accuracy for our scheme. Due to $u(x,0)$ in (5.1) is not smooth enough, in order to observe more than second order accuracy, we modify it as

$$u(x,0) = u_0 \sin\left(2\pi x/L\right)\left(1-\cos\left(2\pi x/L\right)\right)/2. \tag{5.2}$$

Others are the same as in (5.1). We take $\varepsilon = 10/11$ to avoid order reduction from the high order IMEX time discretization. We take mesh sizes with $N_k = 2^k \cdot N_0$, where $k = 0, 1, 2, 3$ and $N_0 = 40$. Reference solutions are computed with $N = 2560$. The errors are computed by comparing the numerical solutions for the pressure p_E to its reference solution. In Table 1, we show the errors and orders at time $t = 0.1$. The order of convergence is between 4 and 5, due to the dominance of spatial errors.

Then we take $\varepsilon = 1/11$ with initial condition (5.1) and compute the solution up to $T = 1.63$ by both "S2T2" and "S4T3" schemes. A reference solution is computed with $N = 2200$. In Figure 1, we compare the reference solution with the numerical ones obtained with $N = 22$ grid points at time $t = 1.63$. We can see that the results of the "S4T3" scheme on the very coarse mesh match the reference solutions better than the "S2T2" scheme.

Example 5.2 (1D shock tube problem). In this example, we consider two 1D shock tube problems in the compressible regime when the Mach number is of $\mathcal{O}(1)$. We take the initial data: one is the Sod problem, where

$$(\rho,u,p) = (1,0,1) \text{ if } x < 0.5; \quad (\rho,u,p) = (0.125,0,0.1) \text{ otherwise}, \tag{5.3}$$

and the other is the Lax problem, where

$$(\rho,u,p) = (0.445,0.698,3.528) \text{ if } x < 0.5; \quad (\rho,u,p) = (0.5,0,0.571) \text{ otherwise}, \tag{5.4}$$

TABLE 1
Example 5.1. *Convergence test for the two colliding acoustic pulses problem with initial condition* (5.1)*, and the velocity is replaced by* (5.2)*.* $t = 0.1$. $\varepsilon = 10/11$.

N	40	80	160	320
L^1 error	1.62E-02	9.97E-04	3.54E-05	1.34E-06
Order	–	4.02	4.82	4.72

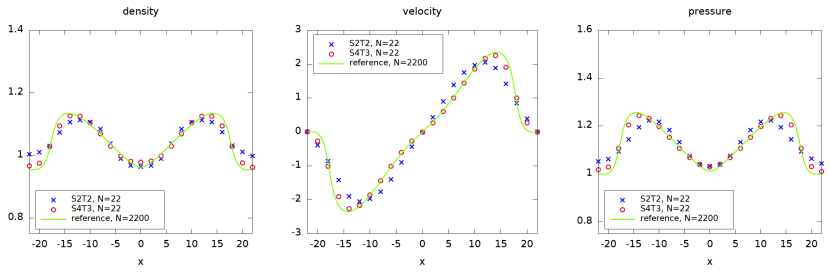

FIG. 1. *Example* 5.1. *Two colliding acoustic pulses with initial condition* (5.1). $t = 1.63$.

both with $\varepsilon = 1$ on the domain $x \in [0,1]$. Reflective boundary conditions are considered and we take $N = 50$. We compute the numerical solution by both "S2T2" and "S4T3" schemes. The results are shown in Figure 2 and compared to the exact solutions. For both the Sod and Lax shock tube problems, the results match the exact solutions very well, which shows that our scheme in the moderate Mach regime (ε of order 1) can capture strong discontinuities without any observable numerical oscillations.

Example 5.3 (2D convergence test). We take the initial data

$$\begin{cases} \rho(x,y,0) &= 1+\varepsilon^2 \sin^2(2\pi(x+y)), \\ \rho(x,y,0)\,u(x,y,0) &= \sin(2\pi(x-y))+\varepsilon^2 \sin(2\pi(x+y)), \\ \rho(x,y,0)\,v(x,y,0) &= \sin(2\pi(x-y))+\varepsilon^2 \cos(2\pi(x+y)) \end{cases} \tag{5.5}$$

on the domain $\Omega = [0,1]^2$ with periodic boundary conditions. Initially we take $p = \rho^\gamma$. We choose $N = N_x = N_y$ and refine the mesh size by $N_k = 2^k \cdot N_0$, for $k = 0,1,2$, with $N_0 = 32$. The numerical errors are computed by comparing the numerical solutions of momentum q_2 to the reference solution, which is computed by the "S4T3" scheme on the mesh $N_x = N_y = 512$. In Table 2, we show the errors and orders at time $t = 0.02$. Around fourth order for $\varepsilon = 1$ and fifth order for $\varepsilon = 10^{-6}$ are observed. For the

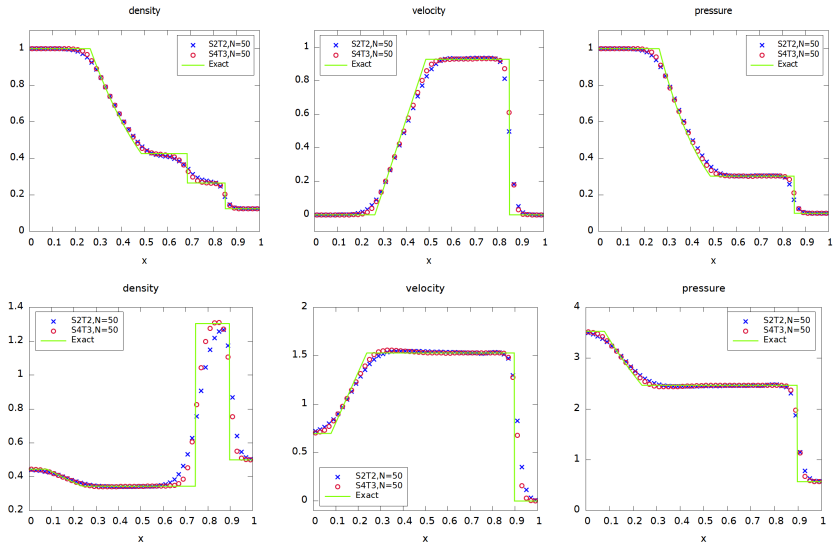

FIG. 2. *Example* 5.2. *1D shock tube problem for* $\varepsilon = 1$. *Top: the Sod problem at* $t = 0.2$. *Bottom: the Lax problem at* $t = 0.16$. *Mesh grid:* $N = 50$. *The solid lines are the exact solutions.*

TABLE 2

Example 5.3. *Convergence test for 2D full Euler equations with initial condition* (5.5) *at* $t = 0.02$. *Errors are computed by comparison with a reference solution.*

	$\varepsilon = 1$		$\varepsilon = 10^{-2}$		$\varepsilon = 10^{-6}$	
N	L^1 error	Order	L^1 error	Order	L^1 error	Order
32	4.64e-03	–	2.45e-03	–	7.26e-05	–
64	2.82e-05	4.05	2.68e-03	–	1.79e-06	5.34
128	1.34e-06	4.39	1.43e-03	0.91	4.81e-08	5.22

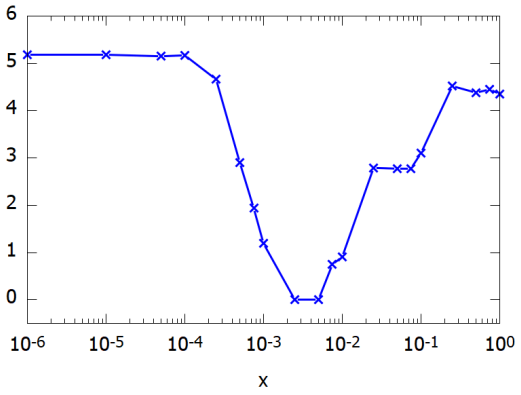

FIG. 3. *Example* 5.3, *2D convergence test for the "S4T3" scheme. Convergence orders versus* ε*'s for* $\varepsilon \in [10^{-6}, 1]$. *As the spatial error dominates, the scheme is observed to have fifth order convergence for small and around fourth order for large values of* ε. *Order degradation is observed for intermediate values of the Mach number.*

intermediate value of $\varepsilon = 10^{-2}$, order reduction is observed. In Figure 3, we display the orders versus ε for $\varepsilon \in [10^{-6}, 1]$, where the order is computed by comparing the errors on the mesh 64×64 and 128×128. Order reduction for intermediate ε's is observed.

Example 5.4 (2D Riemann problem). This is a 2D Riemann problem in the high Mach regime. We take $\varepsilon = 1$ and $\Omega = [-1, 1]^2$. The initial data are defined in four quadrants, which are modified from Configuration 3 in [35] with four shocks,

$$(\rho, u, v, p) = \begin{cases} (1.5, 0, 0, 1.5), & x \geq 0.8, \quad y \geq 0.8; \\ (0.5323, 1.206, 0, 0.3)), & x < 0.8, \quad y \geq 0.8; \\ (0.138, 1.206, 1.206, 0.029), & x < 0.8, \quad y < 0.8; \\ (0.5323, 0, 1.206, 0.3), & x \geq 0.8, \quad y < 0.8. \end{cases} \tag{5.6}$$

The second one is Configuration 5 in [35] with four contact discontinuities, where the initial data are

$$(\rho, u, v, p) = \begin{cases} (1, -0.75, -0.5, 1), & x \geq 0.5, \quad y \geq 0.5; \\ (2, -0.75, 0.5, 1), & x < 0.5, \quad y \geq 0.5; \\ (1, 0.75, 0.5, 1), & x < 0.5, \quad y < 0.5; \\ (3, 0.75, -0.5, 1), & x \geq 0.5, \quad y < 0.5. \end{cases} \tag{5.7}$$

We take mesh size $N_x \times N_y = 400 \times 400$. For this example, four different approaches are compared to the reference solution. The first one is our splitting approach, where we take $\alpha = 1$ in (3.2), using both spatial discretizations ∇_{CW} and ∇_W described in section 3.3 ("A1"); another one uses the same splitting, but replaces ∇_{CW} all by ∇_W ("A2"); the third one has no splitting, namely, we take $\alpha = 0$ in (3.2) and only ∇_W is used ("A3"); the last one is the "S2T2" scheme using the same approach as "A1." In Figure 4, we show the surface plots of the density at $T = 0.8$ for the initial data (5.6). We can see that the solution of A1 is the closest to the reference solution and no obvious oscillations are observed. For the other two approaches, A2 and A3, the

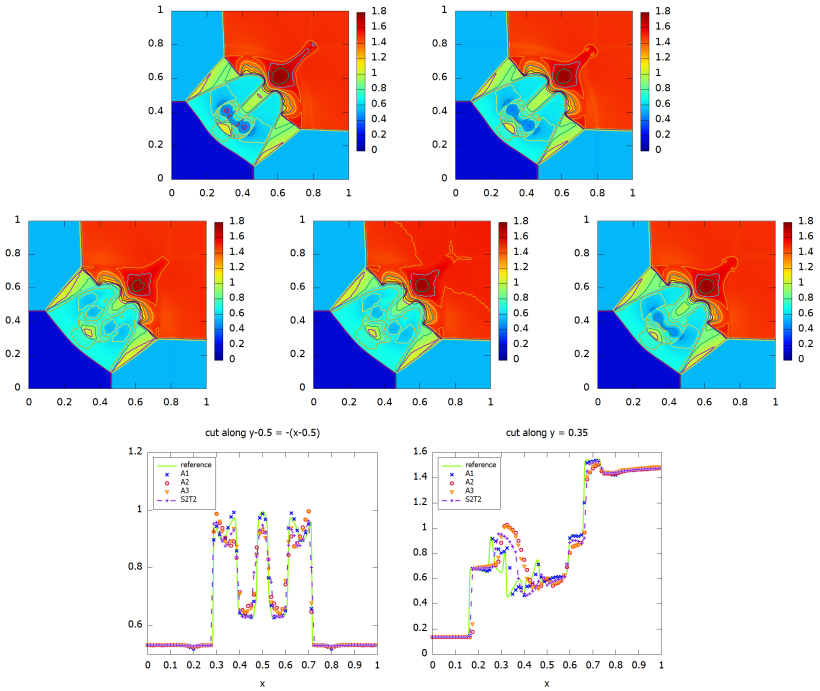

FIG. 4. *Example* 5.4. *Surface and cut plots of the density for* 2*D Riemann problem* (5.6) *at* $T = 0.8$. *Mesh grid:* 400×400. *Top left: reference solution; top right: the approach A*1*, splitting with characteristicwise reconstruction* ∇_{CW}*; middle left: the approach A*2*, splitting with only componentwise reconstruction* ∇_W*; middle middle: the approach A*3*, no splitting; middle right: S*2*T*2*. Bottom are* 1*D cuts of these solutions.*

solutions do not perform well; numerical oscillations can be clearly seen in the middle region. The result of the second order "S2T2" scheme is close to "A1," but it has poorer resolutions. We also show the cutting plots along two different lines. The A1 approach is observed to perform better than the A2 and A3 approaches, and "S2T2" is in between but a little closer to A1, which show the importance of characteristic reconstructions. In Figure 5, we present same results for the 2D Riemann initial data (5.7) at $T = 0.23$. Similar observations can be made.

Example 5.5 (Gresho vortex [39, 9, 8]). This is the time-dependent rotational Gresho vortex problem for the full Euler system. Initially a vortex is centered at $(x_0, y_0) = (0.5, 0.5)$ with radius $R = 0.4$ in the domain $[0, 1]^2$. The initial background state is set as $\rho_\infty = 1$, $\mathbf{u}_\infty = (u_\infty, 0)$, $p_\infty = 1$, $c_\infty = \sqrt{\gamma p_\infty/\rho_\infty} = \sqrt{\gamma}$. The transverse velocity for the vortex is given by

$$u_\theta(r) = \begin{cases} 2r/R & \text{if} \quad 0 \le r < R/2, \\ 2(1 - r/R) & \text{if} \quad R/2 \le r < R, \\ 0 & \text{if} \quad r \ge R, \end{cases} \tag{5.8}$$

and the corresponding velocity components are

$$u(x, y, 0) = u_\infty - \frac{y - y_0}{r} u_\theta(r), \;\; v(x, y, 0) = \frac{x - x_0}{r} u_\theta(r).$$

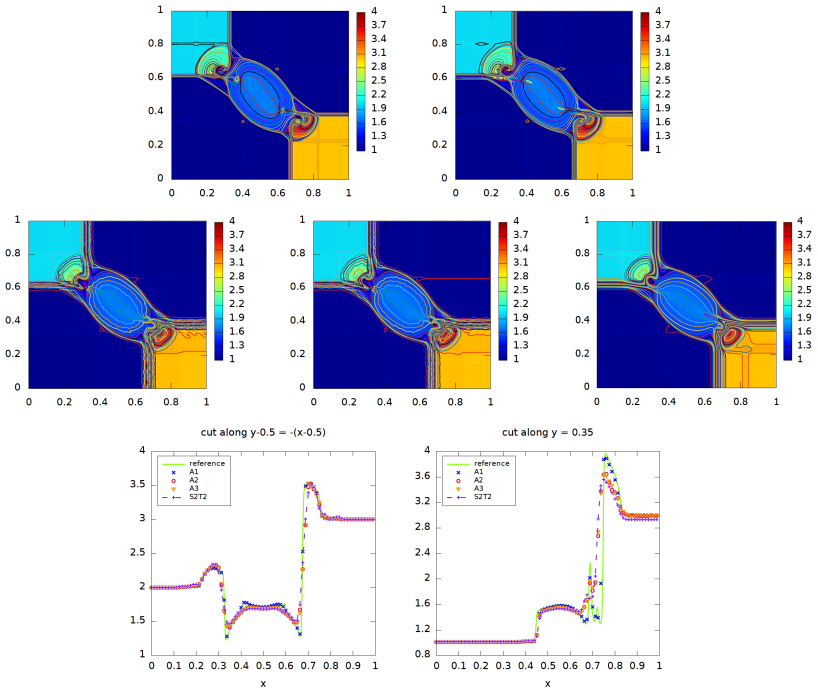

FIG. 5. *Example* 5.4. *Surface plots of the density for* 2*D Riemann problem* (5.7) *at* $T = 0.23$. *Mesh grid:* 400×400. *Top left: reference solution; top right: the approach* $A1$, *splitting with characteristicwise reconstruction* ∇_{CW}; *middle left: the approach* $A2$, *splitting with only componentwise reconstruction* ∇_W; *middle middle: the approach* $A3$, *no splitting; middle right:* $S2T2$. *Bottom are* 1*D cuts of these solutions.*

The centrifugal force is balanced by the pressure gradient, so the (scaled) pressure is given by

$$p(r) = p_\infty + \varepsilon^2 \begin{cases} 2(r/R)^2 + 2 - \log 16 & \text{if} \quad 0 \le r < R/2, \\ 2(r/R)^2 - 4(2r/R + \log(r/R)) + 6 & \text{if} \quad R/2 \le r < R, \\ 0 & \text{if} \quad r \ge R, \end{cases} \tag{5.9}$$

where $r = \sqrt{(x-0.5)^2 + (y-0.5)^2}$. Periodic boundary conditions on both directions are used and the mesh is $N_x \times N_y = 100 \times 100$. The background velocity is $u_\infty = 0.1$ moving in the x-direction, and we take $\varepsilon = 10^{-1}, 10^{-2}, 10^{-6}$. The rotation period is $2\pi/\omega = R\pi$ if $r \le R/2$. We take $T = R\pi$ as one rotating period [8].

We define the ratio between the local and the maximum Mach number as

$$M_{\text{ratio}} = \sqrt{[(u-u_\infty)^2 + v^2]/(\gamma p/\rho)}. \tag{5.10}$$

In Figure 6 (top left), we show the surface plot of M_{ratio} for the initial condition with $\varepsilon = 10^{-2}$, which is very similar for other ε's. As time evolves, the solution will rotate while moving in the x-direction, but its shape will be kept. However, numerically the shape will be damped due to numerical viscosity. This is a standard example to check whether the numerical viscosity greatly depends on the parameter ε or not. For better illustration, we show the cutting plots along $x = 0.5$ at two different times: one

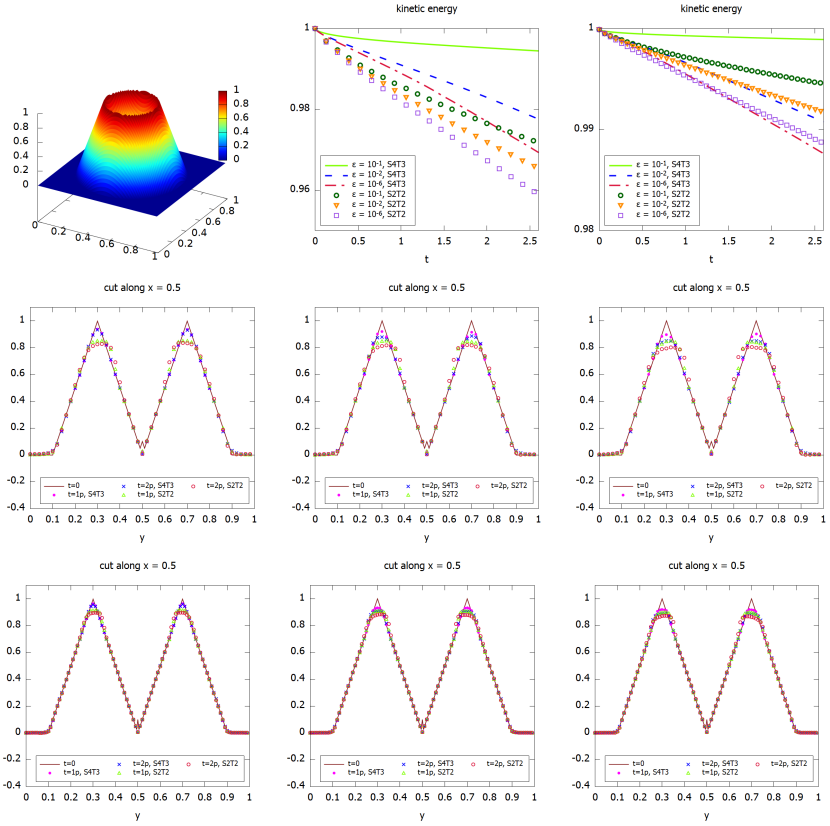

FIG. 6. *Example* 5.5, *Gresho vortex problem. Top left:* M_{ratio} *in* (5.10) *at* $T = R\pi$ *on the mesh grid* 100×100. *Top middle: time evolution of the kinetic energy* (5.11) *relative to its initial value on the mesh grid* 100×100. *Top right: time evolution of the kinetic energy* (5.11) *relative to its initial value on the mesh grid* 200×200. *Middle and bottom: cuts along* $x = 0.5$ *at three different times, initial* ($t = 0$), *one period* ($t = 1p$), *two periods* ($t = 2p$). *The results are shifted to the center by* $-u_\infty t$ *periodically. From left to right:* $\varepsilon = 10^{-1}$, $\varepsilon = 10^{-2}$, $\varepsilon = 10^{-6}$. *Middle: mesh* 100×100; *bottom: mesh* 200×200.

period and two periods, for both schemes "S4T3" and "S2T2," and compare them to the corresponding initial shapes, for $\varepsilon = 10^{-1}, 10^{-2}, 10^{-6}$, respectively. In these plots, the vortex is shifted to the center by $-u_\infty t$ periodically. Two meshes are used: 100×100 and 200×200. We can see that the shapes are preserved relatively well for both "S4T3" and "S2T2" schemes, and the results of "S4T3" are a little better than those of "S2T2." In Figure 6, we also show the time evolution of the averaged kinetic energy, which is defined as

$$\text{kinetic energy} = \sum_{i,j} \left[(u(x_i, y_j, t) - u_\infty)^2 + v(x_i, y_j, t)^2 \right] / N_x N_y. \tag{5.11}$$

We can see the conservation of kinetic energy is well maintained. For a coarse mesh 100×100, the high order scheme "S4T3" preserves the kinetic energy clearly better than "S2T2." Refining the mesh can greatly improve the conservation of the kinetic energy, and the differences between these two methods are reduced, especially for small ε's.

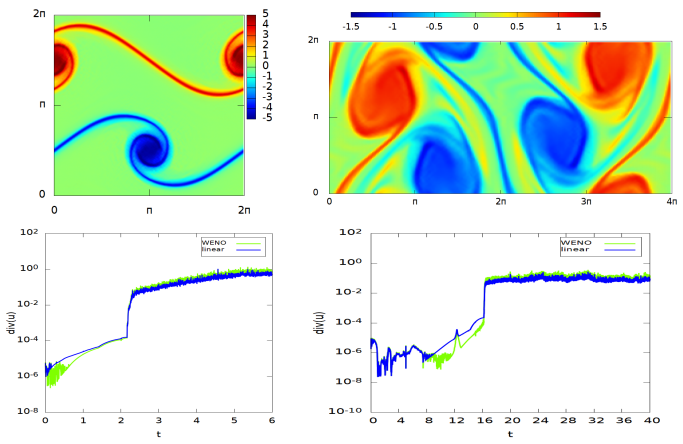

FIG. 7. *Example* 5.6, *the vorticity* $\omega = v_x - u_y$ *and time history of* L^∞ *norm for the divergence* $u_x + v_y$. *Left: the shear flow problem* (5.12) *at* $T = 6$ *with mesh grid* 256×256. *Right: the Kelvin–Helmholtz instability problem* (5.13) *at* $T = 40$ *with mesh grid* 256×128.

Example 5.6 (incompressible flow). Finally we consider two problems in the incompressible flow regime by taking $\varepsilon = 10^{-6}$. One is the shear flow problem on $[0, 2\pi]^2$ with

$$v(x, y, 0) = \delta \cos(x), \quad u(x, y, 0) = \begin{cases} \tanh((y - \frac{\pi}{2})/\rho) & \text{if } y \le \pi, \\ \tanh((\frac{3\pi}{2} - y)/\rho) & \text{if } y > \pi. \end{cases} \tag{5.12}$$

The other is the Kelvin–Helmholtz instability problem [17] on $[0, 4\pi] \times [0, 2\pi]$ with

$$u(x, y, 0) = \cos(y), \quad v(x, y, 0) = 0.03 \sin(0.5x). \tag{5.13}$$

The initial density and pressure for both cases are taken to be 1. For the shear flow problem, we run the solution up to $T = 6$ on a mesh grid 256×256, while $T = 40$ for the Kelvin–Helmholtz instability problem on the mesh grid, $N_x \times N_y = 256 \times 128$. The vorticity $\omega = v_x - u_y$ for both cases is shown in Figure 7, where v_x and u_y are discretized by the fourth order central difference. We observe that it is comparable to the results for the isentropic case as in [8].

We also show the time evolution of the divergence error $u_x + v_y$ for the velocity in Figure 7. The divergence is computed by a fifth order finite difference WENO reconstruction with zero viscosity, which mimics what we have done in the numerical scheme. We also compare it with the linear fourth order central difference discretization. For both cases, the divergence error is increasing with time. When very fine structures are no longer supported by the mesh, the divergence error suffers from a sudden increase. We would remark that when the flow is incompressible or weakly incompressible, without discontinuities in the initial condition, high order linear reconstructions would perform better than WENO reconstructions in preserving the divergence and in resolving solution structures.

6. Conclusion. In this paper we present a high order semi-implicit IMEX-RK WENO scheme for the full compressible Euler equations in the case of all-Mach flows. We combine the semi-implicit IMEX-RK discretization in time with high order finite difference WENO space discretizations. The EOS is treated in a semi-implicit manner, therefore requiring the solution of linearized elliptic systems at each time step.

Characteristic reconstructions are proposed in the semi-implicit framework with a fixed splitting for the pressure. The scheme is proven to be asymptotic preserving and asymptotically accurate in the incompressible limit. Numerical tests have demonstrated the efficiency and effectiveness of our proposed approach.

REFERENCES

[1] S. Boscarino, *Error analysis of IMEX Runge–Kutta methods derived from differential-algebraic systems*, SIAM J. Numer. Anal., 45 (2008), pp. 1600–1621.

[2] S. Boscarino, R. Bürger, P. Mulet, G. Russo, and L. M. Villada, *Linearly implicit IMEX Runge–Kutta methods for a class of degenerate convection-diffusion problems*, SIAM J. Sci. Comput., 37 (2015), pp. B305–B331.

[3] S. Boscarino, R. Bürger, P. Mulet, G. Russo, and L. M. Villada, *On linearly implicit IMEX Runge-Kutta methods for degenerate convection-diffusion problems modeling polydisperse sedimentation*, Bull. Braz. Math. Soc., (N.S.), 47 (2016), pp. 171–185.

[4] S. Boscarino, F. Filbet, and G. Russo, *High order semi-implicit schemes for time dependent partial differential equations*, J. Sci. Comput., 68 (2016), pp. 975–1001.

[5] S. Boscarino, P. G. LeFloch, and G. Russo, *High-order asymptotic-preserving methods for fully nonlinear relaxation problems*, SIAM J. Sci. Comput., 36 (2014), pp. A377–A395.

[6] S. Boscarino and L. Pareschi, *On the asymptotic properties of IMEX Runge–Kutta schemes for hyperbolic balance laws*, J. Comput. Appl. Math., 316 (2017), pp. 60–73.

[7] S. Boscarino, L. Pareschi, and G. Russo, *Implicit-explicit Runge–Kutta schemes for hyperbolic systems and kinetic equations in the diffusion limit*, SIAM J. Sci. Comput., 35 (2013), pp. A22–A51.

[8] S. Boscarino, J.-M. Qiu, G. Russo, and T. Xiong, *A high order semi-implicit IMEX WENO scheme for the all-Mach isentropic Euler system*, J. Comput. Phys., 392 (2019), pp. 594–618.

[9] S. Boscarino, G. Russo, and L. Scandurra, *All Mach number second order semi-implicit scheme for the Euler equations of gas dynamics*, J. Sci. Comput., 17 (2018), pp. 850–884.

[10] W. Boscheri and L. Pareschi, *High order pressure-based semi-implicit IMEX schemes for the 3D Navier-Stokes equations at all Mach numbers*, J. Comput. Phys., 434 (2021), 110206.

[11] J. C. Butcher, *Numerical Methods for Ordinary Differential Equations*, 3rd ed., John Wiley & Sons, New York, 2016.

[12] V. Casulli and D. Greenspan, *Pressure method for the numerical solution of transient, compressible fluid flows*, Internat. J. Numer. Methods Fluids, 4 (1984), pp. 1001–1012.

[13] A. J. Chorin, *Numerical solution of the Navier-Stokes equations*, Math. Comput., 22 (1968), pp. 745–762.

[14] A. J. Chorin and J. Marsden, *A Mathematical Introduction to Fluid Mechanics*, Springer, New York, 1993.

[15] B. Cockburn, C. Johnson, C.-W. Shu, and E. Tadmor, *Advanced Numerical Approximation of Nonlinear Hyperbolic Equations: Lectures Given at the 2nd Session of the Centro Internazionale Matematico Estivo (CIME) Held in Cetraro, Italy*, 1997, Springer, New York, 2006.

[16] F. Cordier, P. Degond, and A. Kumbaro, *An asymptotic-preserving all-speed scheme for the Euler and Navier-Stokes equations*, J. Comput. Phys., 231 (2012), pp. 5685–5704.

[17] N. Crouseilles, M. Mehrenberger, and E. Sonnendrücker, *Conservative semi-Lagrangian schemes for vlasov equations*, J. Comput. Phys., 229 (2010), pp. 1927–1953.

[18] P. Degond and M. Tang, *All speed scheme for the low Mach number limit of the isentropic Euler equations*, Commun. Comput. Phys., 10 (2011), pp. 1–31.

[19] S. Dellacherie, *Analysis of Godunov type schemes applied to the compressible Euler system at low Mach number*, J. Comput. Phys., 229 (2010), pp. 978–1016.

[20] F. Denner, F. Evrard, and B. van Wachem, *Conservative finite-volume framework and pressure-based algorithm for flows of incompressible, ideal-gas and real-gas fluids at all speeds*, J. Comput. Phys., 409 (2020), 109348.

[21] F. Denner, C.-N. Xiao, and B. van Wachem, *Pressure-based algorithm for compressible interfacial flows with acoustically-conservative interface discretization*, J. Comput. Phys., 367 (2018), pp. 192–234.

[22] G. Dimarco, R. Loubère, and M.-H. Vignal, *Study of a new asymptotic preserving scheme for the Euler system in the low Mach number limit*, SIAM J. Sci. Comput., 39 (2017), pp. A2099–A2128.

[23] E. Godlewski and P.-A. Raviart, *Numerical Approximation of Hyperbolic Systems of Conservation Laws*, Springer, New York, 2014.

[24] J.-L. Guermond, P. Minev, and J. Shen, *An overview of projection methods for incompressible flows*, Comput. Methods Appl. Mech. Engrg., 195 (2006), pp. 6011–6045.
[25] J. Haack, S. Jin, and J.-G. Liu, *An all-speed asymptotic-preserving method for the isentropic Euler and Navier-Stokes equations*, Commun. Comput. Phys., 12 (2012), pp. 955–980.
[26] E. Hairer, S. Nørsett, and G. Wanner, *Solving Ordinary Differential Equations: Nonstiff Problems*, Vol. 1, Springer, New York, 1993.
[27] E. Hairer and G. Wanner, *Solving Ordinary Differential Equations* II: *Stiff and Differential Algebraic Problems*, Vol. 2, Springer, New York, 1993.
[28] F. Harlow and A. Amdsen, *Numerical calculation of almost incompressible flow*, J. Comput. Phys., 3 (1968), pp. 80–93.
[29] F. Harlow and A. Amdsen, *A numerical fluid dynamics calculation method for all flow speeds*, J. Comput. Phys., 8 (1971), pp. 197–213.
[30] S. Jin, *Efficient asymptotic-preserving (AP) schemes for some multiscale kinetic equations*, SIAM J. Sci. Comput., 21 (1999), pp. 441–454.
[31] S. Jin, *Asymptotic Preserving (AP) Schemes for Multiscale Kinetic and Hyperbolic Equations: A Review*, Lecture Notes for Summer School on Methods and Models of Kinetic Theory (M&MKT), Porto Ercole, Grosseto, Italy, 2010, pp. 177–216.
[32] S. Klainerman and A. Majda, *Singular limits of quasilinear hyperbolic systems with large parameters and the incompressible limit of compressible fluids*, Comm. Pure Appl. Math., 34 (1981), pp. 481–524.
[33] S. Klainerman and A. Majda, *Compressible and incompressible fluids*, Comm. Pure Appl. Math., 35 (1982), pp. 629–651.
[34] R. Klein, *Semi-implicit extension of a Godunov-type scheme based on low Mach number asymptotics.* I*: One-dimensional flow*, J. Comput. Phys., 121 (1995), pp. pp. 213–237.
[35] P. D. Lax and X.-D. Liu, *Solution of two-dimensional Riemann problems of gas dynamics by positive schemes*, SIAM J. Sci. Comput., 19 (1998), pp. 319–340.
[36] R. J. LeVeque, *Finite Volume Methods for Hyperbolic Problems*, Cambridge texts Appl. Math., 31, Cambridge University Press, Cambridge, UK, 2002.
[37] F. Miczek, F. Röpke, and P. Edelmann, *A new numerical solver for flows at various Mach numbers*, Astronom. Astrophys., 576 (2015), A50.
[38] C.-D. Munz, S. Roller, R. Klein, and K. J. Geratz, *The extension of incompressible flow solvers to the weakly compressible regime*, Comput. Fluids, 32 (2003), pp. 173–196.
[39] S. Noelle, G. Bispen, K. R. Arun, M. Lukáčová-Medvidová, and C.-D. Munz, *A weakly asymptotic preserving low Mach number scheme for the Euler equations of gas dynamics*, SIAM J. Sci. Comput., 36 (2014), pp. B989–B1024.
[40] L. Pareschi and G. Russo, *Implicit-explicit Runge-Kutta schemes and applications to hyperbolic systems with relaxation*, J. Sci. Comput., 25 (2005), pp. 129–155.
[41] J.-H. Park and C.-D. Munz, *Multiple pressure variables methods for fluid flow at all Mach numbers*, Internat. J. Numer. Methods Fluids, 49 (2005), pp. 905–931.
[42] C.-W. Shu, *Essentially non-oscillatory and weighted essentially non-oscillatory schemes for hyperbolic conservation laws*, in Advanced Numerical Approximation of Nonlinear Hyperbolic Equations, Springer, New York, 1998, pp. 325–432.
[43] C.-W. Shu, *High order weighted essentially nonoscillatory schemes for convection dominated problems*, SIAM Rev., 51 (2009), pp. 82–126.
[44] M. Tang, *Second order method for isentropic Euler equation in the low Mach number regime*, Kinet. Relat. Models, 5 (2012), pp. 155–184.
[45] M. Tavelli and M. Dumbser, *A pressure-based semi-implicit space–time discontinuous Galerkin method on staggered unstructured meshes for the solution of the compressible Navier–Stokes equations at all Mach numbers*, J. Comput. Phys., 341 (2017), pp. 341–376.
[46] R. Temam, *Navier-Stokes Equations: Theory and Numerical Analysis*, AMS Chelsea Publishing, Providence, RI, 1984.
[47] E. F. Toro, *Riemann Solvers and Numerical Methods for Fluid Dynamics: A Practical Introduction*, Springer, New York, 2009.
[48] E. Turkel, *Preconditioned methods for solving the incompressible and low speed compressible equations*, J. Comput. Phys., 72 (1987), pp. 277–298.
[49] E. Turkel, A. Fiterman, and B. van Leer, *Preconditioning and the Limit to the Incompressible Flow Equations*, NASA CR-191500, 1993.
[50] C. Viozat, *Implicit Upwind Schemes for Low Mach Number Compressible Flows*, Ph.D. thesis, Inria, 1997.
[51] J. Zeifang, J. Schütz, K. Kaiser, A. Beck, M. Lukáčová-Medvidová, and S. Noelle, *A novel full-Euler low Mach number IMEX splitting*, Commun. Comput. Phys., 27 (2020), pp. 292–320.